THESIS FOR THE DEGREE OF DOCTOR OF PHILOSOPHY

Electrochemical Studies of Quinonoid Compounds for Aqueous Organic Redox Flow Batteries

CEDRIK WIBERG

Department of Chemistry and Chemical Engineering

CHALMERS UNIVERSITY OF TECHNOLOGY

Gothenburg, Sweden 2020

Electrochemical Studies of Quinonoid Compounds for Aqueous Organic Redox Flow Batteries
CEDRIK WIBERG
ISBN 978-91-7905-338-3

Doktorsavhandlingar vid Chalmers tekniska högskola
Ny serie nr 4805
ISSN 0346-718X

Department of Chemistry and Chemical Engineering
Chalmers University of Technology
SE-412 96 Göteborg
Sweden
Telephone + 46 (0)31-772 1000

Cover: A battery with a symbolic environmental synergy.
Artist: Mariza Mone

Chalmers Digitaltryck
Göteborg, Sweden 2020

Electrochemical Studies of Quinonoid Compounds for Aqueous Organic Redox Flow Batteries

CEDRIK WIBERG
Department of Chemistry and Chemical Engineering
Chalmers University of Technology

Abstract

In the current times of uncertainty in face of climate change, sustainable energy-related technologies are developed with urgency. A candidate of special interest is Aqueous Organic Redox Flow Batteries (AORFB), whose utility depends heavily on the organic molecules used. In this work, the archetypical AORFB molecule, 9,10-anthraquinone-2,7-disulfonic acid (AQDS) was investigated in aqueous solution using a combination of electrochemistry and diffusion NMR in order to show that its battery performance is hampered by self-association. The self-associative species are not reduced in aqueous solution, and consequently, only a fraction of the capacity is redox-accessible in the oxidized state. The self-association was shown to be strong enough that only 27% of the molecules in a typical 1 M AQDS, pH 0 sulfuric acid electrolyte occur in a redox-accessible monomeric form. Furthermore, a class of molecules called naphthalene diimides (NDIs) were for the first time investigated electrochemically in aqueous solution and found to have appealing properties for application in AORFBs. One of the simplest naphthalene diimides, in this work called 2H-NDI, was examined by combining rotating disk electrode voltammetry, ^{1}H-NMR spectroscopy, and diffusion NMR, to show that 2H-NDI also self-associates, and has an equilibrium constant for dimer formation of approximately 150 M^{-1}. The 2H-NDI dimer was shown to have a decreased electrochemical activity, but in contrast to AQDS, the dimerization did not negatively affect bulk electrolytic behavior, likely due to a larger dimer dissociation rate constant. Apart from 2H-NDI, eight other naphthalene diimides, differentiated by the substituent on the naphthalene core, were studied using density functional theory (DFT). The NDIs were disubstituted with Br, F, NH_2, NO_2, $N(CH_3)_2$ (called DMA), OH, and CN, for which reduction potentials and pK_a values as well as oxidative and reductive pathways were predicted. These findings were used to give mechanistic insight on experimental work on 2H-NDI, 2Br-NDI and 2DMA-NDI, the last of which has a complex reduction mechanism due to the possibility of being protonated at the amine substituents. Five pH neutral aqueous redox flow batteries using equimolar solutions of 2H-NDI or 2DMA-NDI coupled with 1,1'-bis[3-(trimethylammonio)propyl]ferrocene (BTMAP-Fc) were assembled and studied. In 1 M potassium chloride and 0.5 M potassium phosphate, two batteries with 50 mM 2H-NDI/BTMAP-Fc or 2DMA-NDI/BTMAP-Fc showed appreciable capacity losses while cycling. However, when instead using 1 M ammonium chloride and 0.5 M ammonium phosphate as the supporting electrolyte, a battery with 50 mM 2H-NDI/BTMAP-Fc displayed a coulombic efficiency of 99.92(2)%, an energy efficiency of 83% at 10 mA cm^{-2}, and extraordinarily, no significant decrease in capacity over 320 cycles. At the same current density, 50 mM 2DMA-NDI/BTMAP-Fc showed a coulombic efficiency of 100.00(5)%, an energy efficiency of 90%, and similar to 2H-NDI/BTMAP-Fc, no capacity decrease was detected over 320 cycles, demonstrating two of the most stable redox flow battery chemistries to date.

Keywords: Naphthalene Diimides, Electrochemistry, Quinones, Self-association

List of Publications

I **Dimerization of 9,10-Anthraquinone-2,7-Disulfonic Acid (AQDS) and its Impact on Aqueous Redox Flow Battery Performance**
Cedrik Wiberg, Thomas J. Carney, Fikile Brushett, Elisabet Ahlberg and Ergang Wang
Electrochimica Acta 2019, *317*, 478-485.

II **Electrochemical Evaluation of Napthalene Diimide (NDI) for Aqueous Redox Flow Batteries**
Cedrik Wiberg, Francis Owusu, Ergang Wang and Elisabet Ahlberg
Energy Technology 2019, *7*, 190846.

III **The Electrochemical Response of Core-functionalized Naphthalene Diimides (NDI) – A Combined Computational and Experimental Investigation**
Cedrik Wiberg, Michael Busch, Lars Nordstierna and Elisabet Ahlberg
Submitted manuscript.

IV **Naphthalene Diimides (NDI) in Highly Stable pH-Neutral Aqueous Organic Redox Flow Batteries**
Cedrik Wiberg, Lars Nordstierna and Elisabet Ahlberg
Manuscript.

Publication not included in the thesis

A Memristive Element Based on an Electrically Controlled Single-Molecule Reaction
Haipeng B. Li, Behabitu E. Tebikachew, Cedrik Wiberg, Kasper Moth-Poulsen and Joshua Hihath
Angewandte Chemie International Edition in English 2020, *59*, 2-8.

Contribution Report

I All experimental work and data processing. Writing of the manuscript as first author.

II Supervision of master student who did much of the synthesis and a minor part of the electrochemistry. Remaining synthesis, electrochemistry experiments and all of the data processing. Writing of the manuscript as first author.

III All experimental work excluding DFT and simulations. All of the data processing and writing of the manuscript as first author.

IV All experimental work, data processing, and writing of the manuscript as first author.

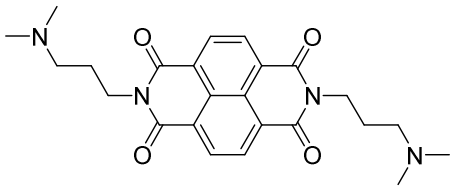
2H-NDI

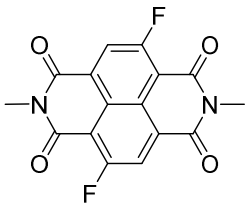
F
F
2F-NDI

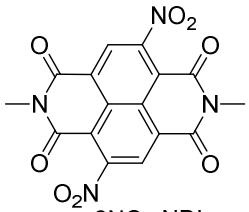
NO2
O2N
2NO2-NDI

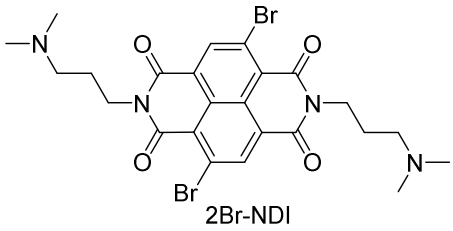
Br
Br
2Br-NDI

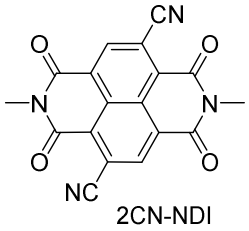
CN
NC
2CN-NDI

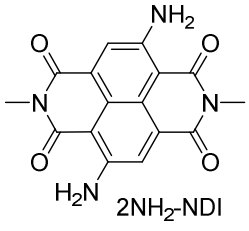
NH2
H2N
2NH2-NDI

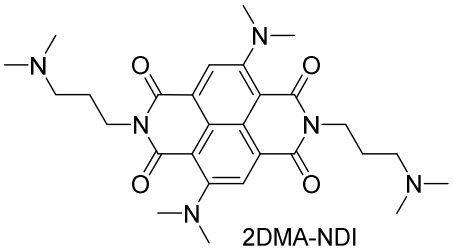
2DMA-NDI

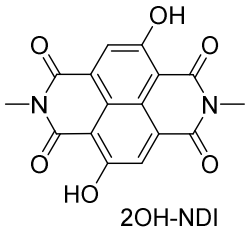
OH
HO
2OH-NDI

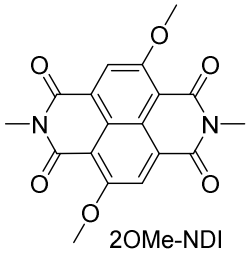
O
O
2OMe-NDI

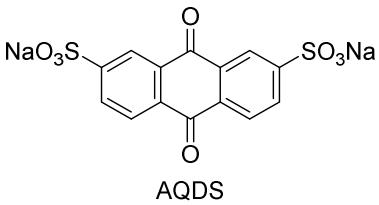
NaO3S
SO3Na
AQDS

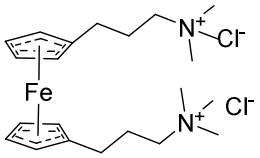
Fe
Cl-
Cl-
BTMAP-Fc

Table of Contents

Sections 2.3, 2.4, and parts of Section 3 are modified forms of those presented in the licentiate thesis by the same author.[1]

1 Scope and Outline

This doctoral thesis focuses on the development and electrochemical behavior of organic molecules for aqueous organic redox flow batteries. 9,10-Anthraquinone-2,7-disulfonic acid and naphthalene diimides (NDIs) were chosen as molecules of interest, with special focus directed on the latter. Establishing a good understanding of the fundamental chemistry and electrochemistry of a molecule was considered a highly necessary step prior to studying it in the applied setting of redox flow batteries. Electrochemical experiments were carried out both at low concentrations, supported by density functional theory, to understand the electrochemical mechanisms under ideal conditions, and at high concentrations, supported by nuclear magnetic resonance spectroscopy, in order to gain knowledge about the self-associative effects on the analyte molecules.

In the final part of the project, the understanding of the fundamental chemical and electrochemical behavior of NDIs is used to optimize the performance of different NDI species in a redox flow battery setup.

2 Introduction

In the end of the 19th century, Svante Arrhenius published an in-depth research article in which through many experiments, handwritten graphs and manually printed data tables, he painstakingly showed that carbon dioxide has a strong tendency to absorb sunlight.[2] This was arguably the first notion of the greenhouse effect and of global warming.

2.1 Carbon Dioxide and Global Warming

Seen in Figure 2-1a are the atmospheric carbon dioxide levels over the last two thousand years.[3, 4] The data from the latter part of the figure is correlated with the measured global temperature anomaly, which is normalized against the years 1951 to 1980, see Figure 2-1b.

The question arises whether the recent development is anthropologic or simply part of Earth's natural climate cycling, as the global temperature is known to have fluctuated significantly during the last few hundreds of millions of years.[5, 6] Arrhenius discoursed this as well, and showed that an increase of the atmospheric carbon dioxide concentration caused by the "combustion and decay of organic bodies" of between 2.5 and 3 times will lead to the arctic regions seeing a temperature increase of about 8-9 °C. He concludes his warning about the correlation between carbon dioxide and global warming with "I should certainly not have undertaken these tedious calculations if an extraordinary interest had not been connected with them". Sadly, the carbon dioxide levels have increased by more than 60% since 1958, and the current levels have reached 414.4 ppm as of July 2020 – a number by far surpassing anything seen in the last 800 000 years.[7, 8]

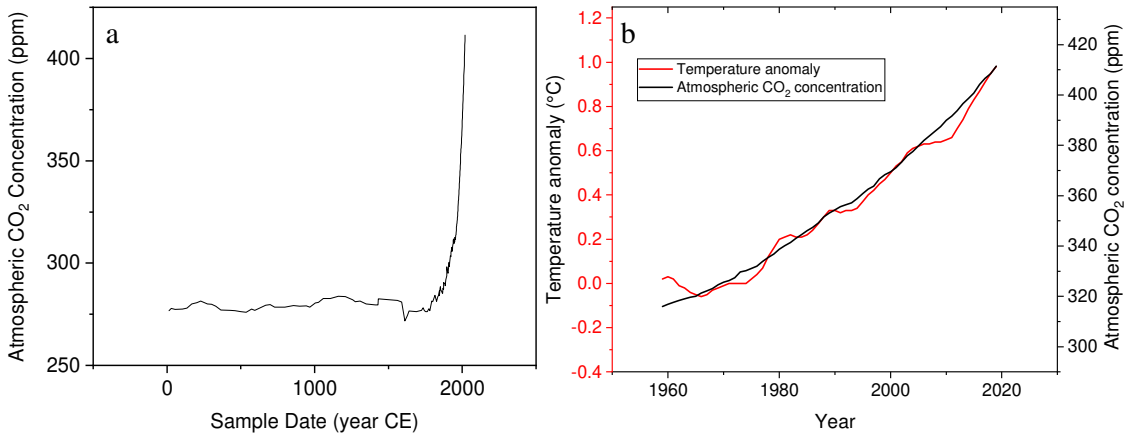

Figure 2-1: a) Plot of carbon dioxide levels with data from year 0-1958 acquired from drilled ice cores,[3, 4] and 1958-2019 is measured at the Mauna Loa observatory.[8] b) Correlation between CO_2 and temperatures measured by NASA.[9]

The current global temperature anomaly is approximately 1 °C, and 19 of the 20 warmest years since 1880 all have occurred since 2001, with 1998 being the exception.[9] Unfortunately, the impact of global warming is not limited to lines on a graph or an abstract sense of foreboding. Between September 2019 and January 2020, which is only a portion of the Australian fire season, 5.8 million hectares, or 21% of the Australian forested area burned.[10] Not only did the fires release vast amounts of carbon dioxide into the atmosphere, experts at the University of Sydney[11] and the World Wildlife Foundation (WWF) estimated a death toll of over a billion animals.[12]

Most of our planet's stored terrestrial carbon is found in the upper parts of the northern hemisphere, where record-high temperatures have recently been reported.[13] Siberia is one geographic area particularly prone to forest fires due to its increasing aridity, large areas of forest, and very limited firefighting capability.[13, 14] Soot released from boreal fires is deposited on arctic glaciers and in turn decreases the albedo of the substrate snow and ice, thus snowballing the thawing of the arctic permafrost.[15] The decrease of the permafrost's surface area further decreases Earth's albedo while also releasing carbon into the atmosphere. Permafrost zones are estimated to contain $1.5 \cdot 10^{12}$ tons of carbon, roughly twice the amount which is currently present in the atmosphere.[14]

The above examples are a few of many climate warming feedback mechanisms which are continuously uncovered,[16] and the need to assuage climate change by reducing greenhouse gas (GHG) emissions is unarguable. In the United States, the transportation sector stands for the largest portion of GHG emissions by 28% of the total, which narrowly exceeds the electricity sector's 27%.[17] In order to decrease GHG emissions, a central strategy is to electrify the transportation sector, which correspondingly will expand the electricity sector, making electricity generation from renewable energy sources (RES) vital.

2.2 Renewable Energy Sources and Energy Storage

In 2019, 27% of the global consumed electricity was produced from RES, where 16% comprised hydropower, 6% wind power and 3% solar.[18] Although hydropower has the most widespread use, its total installed capacity has only increased by about 30% in the last decade, while solar and wind capacities have expanded exponentially since the 1990's.[19-21] In 2013, an equal amount of power capacity of hydro, wind and solar electricity generation was added - between 35 and 38 GW. Conversely, in 2019, added hydropower capacity decreased to well below 20 GW, while capacities for wind and solar increased by 60 GW and 115 GW respectively.[18]

One of the main obstacles to the continued growth of renewably sourced electricity is the intermittency of the sun and the wind. Thus, in countries where hydropower is not ecologically feasible, reaching a large portion of electricity generation from RES is only possible if coupled with energy storage.[22, 23]

In 2019, the installed stationary energy storage capacity amounted to 30 GWh on a global basis and was projected by the International Renewable Energy Agency (IRENA) to increase to 370 GWh by 2030, and 3400 GWh by 2050.[24] In these projections, the global temperature would rise by 2.5 °C, which is significantly above the desired values. In contrast, a so-called transformative energy scenario was also given, where the temperature increase is limited to well below 2 °C, and in this scenario, 3400 GWh would be required by 2030, and 9000 GWh by 2050. If the stationary energy storage capacity is to increase by between 20 and 300 times

by 2050, the choice of storage technology is crucial. In 2017, almost all of the added stationary chemical energy storage capacity was in the form of lithium-ion batteries (LIBs). When combined with the electric vehicle sector, which is the main sector for LIBs, the combined scale for the technology will be enormous.[24] LIBs have several drawbacks that motivate the development of other, more environmentally friendly energy storage technologies. More information on this topic is found in Section 2.5.

As an alternative to LIBs for large-scale stationary energy storage, redox flow batteries (RFBs) are often mentioned as an interesting candidate. RFBs show promise to hold many advantages over LIBs including increased safety of operation, cycle longevity and lower cost.[25]

2.3 Redox Flow Batteries

RFBs, which are sometimes referred to as regenerative fuel cells, consist of two separate tanks containing electrolyte solutions that are pumped through fuel cell-like reactors upon operation.[26] The electrolyte solutions are typically aqueous and contain the redox-active molecules (RMs) as well as a supporting electrolyte, often sulfuric acid.[27, 28] The solutions in the tanks contain different RMs, alternatively the same RM but at differing oxidation states. The difference in reduction potential between the RMs in the determines the voltage of the battery. The solution containing the molecule with the more negative redox potential is called negative electrolyte, negolyte or catholyte, and the solution containing the molecule with the more positive redox potential is called positive electrolyte, posolyte or anolyte. The supporting electrolyte serves to make the solution ionically conductive and to provide the system with mobile charge carriers.

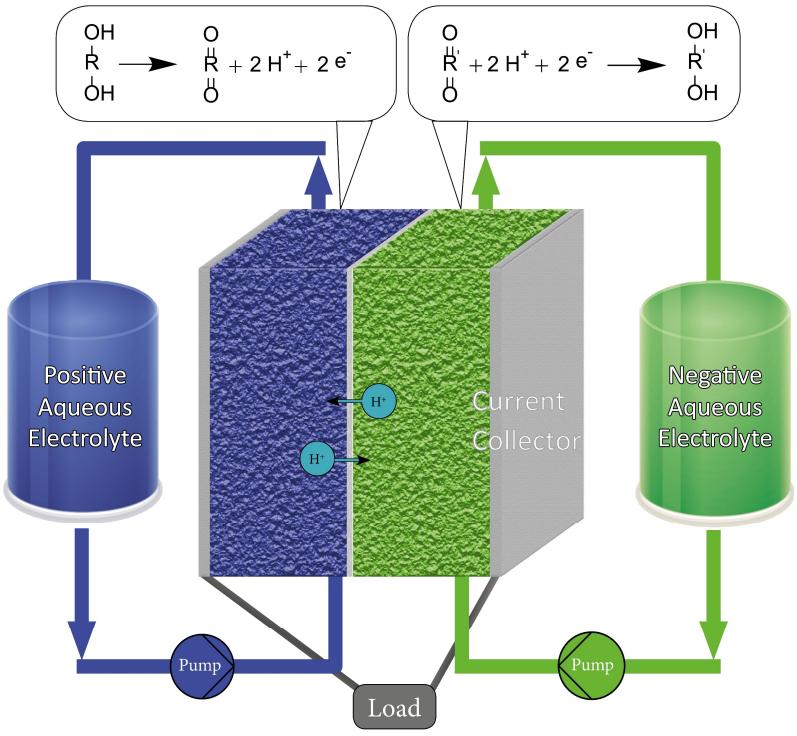

Figure 2-2: A schematic of an AORFB.

Figure 2-2 shows the components of an aqueous organic redox flow battery (AORFB). During discharging, the electrolyte solutions are pumped through an electrochemical cell consisting of two porous electrodes, which are typically separated by an ion-selective membrane. The

electrodes are generally graphite-based, and designed to have a large specific surface area, high mechanical stability and high conductivity.[29] The choice of membrane will vary strongly depending on the electrolyte,[30-32] but Nafion ion-exchange membranes are the most commonly used ones.[32] Upon operation, the molecule in the anolyte - once it reaches the surface of the porous electrode - gets oxidized and gives off an electron which is conducted through an external circuit and used as electricity. At the same time, the catholyte receives an electron from the porous electrode on the cathodic side, and thus gets reduced. Since an electron has effectively been transported from one side of the cell to the other, a charge imbalance has arisen. To negate this, an ion migrates through the membrane from the one electrolyte side of the electrochemical cell to the other. Which ion migrates will depend on the electrolyte solution and the membrane.

The power capacity of a redox flow battery is determined by the amount of material dissolved in the solution, the amount of solution and the voltage. As such, capacity fade in redox flow batteries usually originates either from chemical degradation of the RMs (especially in the case of organic redox flow batteries) or from crossover of the RMs through the membrane.[26, 33]

Having a setup with the RM stored in tanks and the redox reaction occurring in cells that are separated from the tanks means that the power and capacity of the system can be scaled independently. If more storage capacity (kWh) is desired, the tanks can be expanded and filled with more electrolyte solution, while if a higher power output (kW) is required, the size or number of the electrochemical cells can be increased, allowing for faster charging and discharging. This characteristic makes flow batteries well-suited for large-scale grid-connected energy storage applications, as the system can be tailored for the specific demands of each deployment. The modular design of the system allows for easy maintenance or replacement of each component, which enables more efficient use of resources. This can be considered a significant advantage over the currently used lithium ion batteries, which typically contain large amounts of aluminum, cobalt, lead and lithium that are seldom recycled.[34, 35]

Finally, the use of aqueous electrolytes makes the system inherently nonflammable and less toxic, compared to LIBs that have organic solvents. As a consequence, they are known to suffer from exothermic chain reactions due to the decomposition of the lithium oxide in a reaction that releases oxygen which can lead to severe fire and explosion hazards.[36-38]

Current commercial redox flow systems include all-vanadium,[27] zinc-bromide,[39] and iron-chromium technologies,[40] with the vanadium-based setup having reached by far the highest level of market maturity among the three.[27, 39, 40] The all-vanadium redox flow battery (VRFB) was first successfully demonstrated in 1988 by Rychcik and Skyllas-Kazacos,[27] and routinely offers lifetimes in the range of 20 000 cycles due to the possibility of remixing the two vanadium species in order to counteract the effect of crossover of redox-active molecules. As there is little chemical degradation of the vanadium species, the VRFBs suffer only a very small capacity fade over time. The biggest hurdle to their market penetration is the limited and volatile supply of vanadium.[41]

2.4 Organic Redox Flow Batteries

Organic redox flow batteries can be categorized by the solvent used: aqueous or non-aqueous.

2.4.1 Aqueous Organic Redox Flow Batteries

One of the most promising energy storage candidates to clear the aforementioned challenges of performance, cost and environmental sustainability are aqueous organic redox flow batteries.[30, 42-48] Due to the possibility to tune the electronic properties of a molecule by chemical functionalization, much work is being done on designing conjugated organic RMs. By adding groups that increase polarity or charge to the molecule, the aqueous solubility can be improved, and by adding electron-donating or electron-withdrawing groups to the conjugated system, the reduction potential can be shifted to more negative or positive values respectively.[49, 50] Organic molecules also have the advantage that they benefit from large scale production,[51] thus avoiding the material scarcity issues that both VRFBs and LIBs suffer from. In 2014, a seminal article reported a redox flow battery employing 9,10-anthraquinone-2,7-disulfonic acid (AQDS) on the negative side, and HBr on the positive side, displaying excellent performance in terms of cycling stability and energy efficiency.[28] However, AQDS suffers from a low capacity utilization[52, 53] and a relatively positive reduction potential, leading to a low battery voltage. AQDS shows close to ideal electrochemistry at a low concentration but deviates from ideality at increasing concentrations, underlining the need to investigate the concentration-dependent behavior of candidate organic molecules.

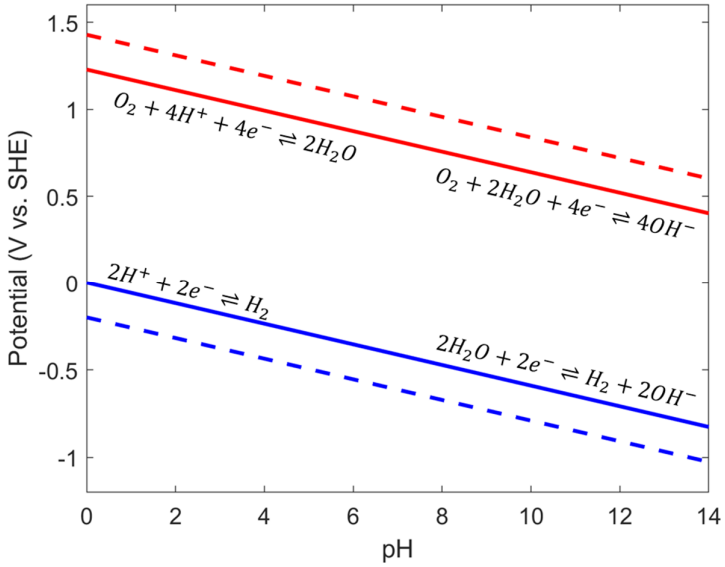

Figure 2-3: Pourbaix diagram of the electrolysis of water. The solid lines show the thermodynamic reduction potentials of the HER and ORR, and the dashed lines show that the range can be extended slightly for graphite electrodes due to sluggish kinetics.

Since then, numerous organic molecules, often quinones, have been considered for use in AORFBs, with varying performance.[25, 47, 49, 50, 54-58] The design challenge is to find molecules that have reversible reductions with potentials close to either extremes of the electrochemical stability window of water. If the molecule has one or more reduction potentials that are too negative or positive, the hydrogen evolution reaction (HER) or the oxygen reduction reaction (ORR) will take place instead of the reduction of the RM, see Figure 2-3. Both the HER and ORR contribute to changing the pH of the solution as well as decreasing the efficiency of the battery. Since the kinetics of the parasitic reactions are quite slow on graphite electrode surfaces, however, the range of the potentials can be extended slightly, indicated by the dashed lines in Figure 2-3.

Apart from having a suitable reduction potential, the molecule needs to have a water solubility in the range of 1 M if it contributes with two electrons per molecule.[44, 45] Furthermore, it needs to have excellent chemical stability at all states of charge,[59] be cheap, non-toxic and environmentally friendly to produce.

One type of molecule that has received little consideration but has the potential to fulfil the above requirements is naphthalene diimides (NDI). NDIs consist of an aromatic naphthalene core, through which the electronic and chemical properties of the molecule can be tuned by chemical functionalization.[60, 61] The imide part of the molecule, which comprises two double-bonded oxygen atoms on either side of a nitrogen atom gives the molecule quinonoid functionality. In other words, upon reduction, the imide oxygen atoms are converted to hydroxyls or alkoxides depending on the pH, analogously to quinones. Different substituents can be chosen on the imide nitrogen, conferring properties mainly relating to solubility and self-association.[60, 62] The electronic tunability of NDIs, combined with their relatively uncomplicated synthetic routes make them an interesting candidate for AORFBs.[63, 64]

2.4.2 Non-aqueous Organic Redox Flow Batteries

Non-aqueous organic redox flow batteries often employ acetonitrile, dimethyl carbonate, diethyl carbonate, propylene carbonate or a mixture of them as solvent. The use of organic solvents opens up the possibility to choose RMs with a wider range of reduction potentials, due to the wider electrochemical stability windows for organic solvents, and cell voltages upwards of 4 V are possible.[65] However, the advantage of a significantly higher cell voltage is balanced by the decreased electrical conductivity of the electrolyte, the use of expensive and often fluorinated supporting salts, decreased RM solubility in the solvent, flammability, solvent cost, and RM stability issues.[44, 65, 66]

2.5 Metals Versus Organic Molecules in Energy Storage

In order to meet the ambitious energy storage growth targets, thought must be placed on the supply safety of the component materials.

Already at present, conventional metal-based battery technologies generally have material supply dependencies that complicate widespread environmentally friendly energy storage. In LIBs, a number of different chemistries are used, based on the application. Generally, the anode consists of graphite into which the lithium ions are intercalated, whereas the cathode is a lithium oxide. Among the most commonly used cathodes are:[67]

- LCO – Lithium Cobalt Oxide, $LiCoO_2$
- NMC – Lithium Nickel Manganese Cobalt Oxide, $Li(Ni_xCo_yMn_z)O_2$
- LFP – Lithium Iron Phosphate, $LiFePO_4$
- LMO – Lithium Manganese Oxide, $LiMn_2O_4$

Lithium is associated with some supply risk due to the rapidly increasing demand, but is generally considered a smaller viability than the other metals.[68-70] Cobalt, for instance, is considered problematic due to its toxicity, scarcity and concentrated localization around central Africa. Roughly half of the World's cobalt supply is used for battery production[71] and the Democratic Republic of Congo (DRC) is behind 60% of the total cobalt mining – a number forecasted to exceed 70% by 2026.[71] Sadly, 15-20% of the mining production in the DRC is so-called artisanal mining,[71] which is associated both with child labor and great health risks for the workers.[72]

In 2015, it was estimated that 43% of the global cobalt production was a byproduct of copper mining, and 44% from nickel mining, although it should be noted that these numbers may have decreased the last half-decade due to the fact that the use of cobalt grows faster than the use of copper and nickel. Consequently, boycotting cobalt from the DRC will likely only have a small impact on the artisanal mining activities, and possibly exacerbate the political situation in the country. The concentration of the cobalt production in an area of such political instability has historically led to considerable price volatility for the metal. Apart from the 1970s cobalt crisis, recent years saw the price of cobalt increase by three times between 2015 and 2018.[73] The popular LCO and NMC chemistries are among the technologies with the highest cobalt content, but efforts to replace cobalt with nickel have been undertaken.[36] This is perhaps mainly due to safety concerns regarding the lithium-cobalt-oxides, which have a relatively low thermal stability and which are prone to thermal runaway reactions compared to other typically used lithium oxides.[36, 38] In the regards of supply safety, the replacement of cobalt with nickel seems to be replacing one problem with another, as there is considerable supply risk associated with nickel as well.[69]

A similar case can be found for vanadium flow batteries, in which both the positive and the negative electrolyte comprise vanadium. For a typical energy-to-power (E/P) ratio of 4, the vanadium comprises 40-50% of the total system cost.[74] This is, of course, heavily dependent on the price of vanadium at the time of assessment, but simultaneously points at the technology's sensitivity to raw material price fluctuations. At the same time, 91% of the global vanadium production is used in steel applications and it is thus relatively insensitive to increases in demand due to increased VRFB deployment.[75]

Summarily, the price – and thus the extent of deployment – of metal-based batteries are all heavily dependent on a number of resources that are persistently volatile in supply.

In contrast, organic molecules consist of hydrogen, carbon, nitrogen, sulfur and oxygen which are all highly abundant elements.[76] Every organic molecule has a unique synthesis route, and therefore a different set of material dependencies. However, most ORFBs use aromatic compounds as active materials with a core consisting of either benzene, naphthalene or anthracene,[57] all of which are fossil components such as coal tar. Looking at naphthalene, it is produced by fractional distillation of coal tar which initially contains about 10-11% naphthalene and has a cost of around 0.77 €/kg (0.84 $/kg).[51] Anthracene occurs in oil tar as well, but in a lower concentration, and is thus more expensive, and a price of 1.84 €/kg (2 $/kg) has been estimated.[51] It has been estimated that the cost of the organic molecules for aqueous organic flow batteries should preferably be less than 4.60 €/kg (5 $/kg).[44] In this regard, there is a principal difference between metals and organic molecules - the economy of scale. Heavily increasing the production volume of metals leads to political, geological, environmental and moral issues, whereas increasing the production volume of organic materials unfailingly leads to a price closer to the raw material price[51] and to benefits in environmental benignity.

3 Theory

The content in the present chapter serves to give the reader an introduction to the techniques used in the thesis. While by no means exhaustive, the chapter is meant to give the reader the necessary background knowledge to follow the results and discussion presented in Chapter 4.

3.1 Cyclic Voltammetry and Rotating Disk Electrode Voltammetry

Cyclic voltammetry (CV) is arguably the electrochemist's most commonly used analytical tool to electrochemically characterize a molecule or system. It is a comparably simple method to set up, and a wealth of information can be obtained if performed and interpreted properly.[77] In some cases, CV can be complemented with rotating disk electrode (RDE) voltammetry in order to acquire additional information about the system, often related to diffusion and kinetics.[78, 79] For both methods, as well as for most other electrochemical systems, the setup comprises a working electrode, a counter electrode and a reference electrode.[80] Very little current is passed through the reference electrode, which serves to give the system a constant potential to which the potential of the redox reaction can be related. Most of the time, the redox reaction of interest takes place at the surface of the working electrode. However, any electron moving into or out of the working electrode means that another electrode must do the opposite operation at the counter electrode. In RDE, the working electrode is rotated at a set of different rates, which provides the electrode surface with a steady stream of new material, the amount of which depends on the rotation rate.

Figure 3-1a shows a CV and RDE sweep for 1 mM AQDS in a slightly alkaline sodium carbonate buffer solution. In these conditions, the system behaves ideally and serves as a good model system. Beginning at a more positive potential than what is required to reduce the molecule, the potential is swept linearly with a set rate (called sweep rate or scan rate). Eventually, when reaching a sufficiently negative potential, the material at the electrode surface starts to be reduced, and a negative current is generated. Consequently, a concentration difference is established against the bulk concentration and unreduced material will start diffusing from the bulk solution towards the electrode surface according to Fick's law of diffusion.[81] Continuing the potential sweep in the negative direction, the reductive current increases until reaching a maximum, signifying that the rate of reduction has surpassed the rate of diffusion, and that the concentration of redox-active material at the electrode surface at this point is zero.

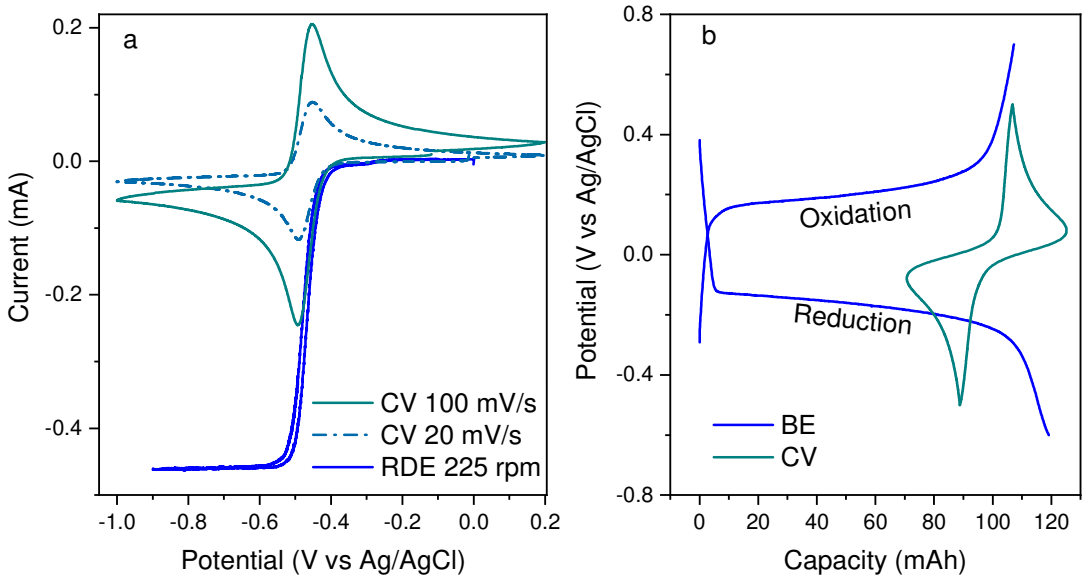

Figure 3-1: a) CVs and RDE of 1 mM AQDS in pH 9.76 sodium carbonate buffer, b) BE and CV of 50 mM AQDS in 1 M H_2SO_4.

For the CV case, if a faster sweep rate is used, the active material at the surface is depleted more quickly, resulting in the formation of a larger concentration gradient, which in turn yields higher peak maxima. The peak height is thus a measure of the concentration and diffusivity of the active species, which is seen in the Randles-Sevcik equation for a reversible electron transfer reaction:[81-83]

$$i_p = 0.4463nFAC\left(\frac{nFvD}{RT}\right)^{\frac{1}{2}}, \qquad 1$$

where i_p is the peak current, n the number of electrons, F the Faraday constant, A the electrode area, C the concentration, v the sweep rate, D the diffusion coefficient, R the gas constant and T the temperature.

Continuing past the maximum, the current decays as the concentration gradient between the surface and the bulk solution gradually decreases and the diffusion rate of unreduced material is lowered. After the last reduction reaction of interest has run its course, the direction of the sweep is reversed, and the reduced species are oxidized back, unless they have taken part in some external electrochemical or chemical reaction during the time that has passed since they were reduced. The peak to peak potential separation between the reduction peak and the returning oxidation peak can give information regarding the number of electrons and the electron transfer rate constant.

In the RDE case, the rotation rate determines the rate at which new material is transported to the surface, and typically, a large enough solution volume is used that the bulk concentration is unaffected by the redox reactions. In contrast to CV, upon changing the potential to a value negative enough to reduce all the material at the electrode surface, a current plateau is reached. At this point, this constant current is only determined by the rate at which new material can reach the electrode surface and is termed the *diffusion-limited* or *mass transfer-limited current.* From this the diffusivity of the molecule, D, as well as the number of electrons, n,

concentration, C, angular rotation rate, ω and kinematic viscosity, ν, can be related, according to the Levich Equation:[81, 83]

$$i_l = 0.62nFA_{RDE}CD^{\frac{2}{3}}\omega^{\frac{1}{2}}\nu^{-\frac{1}{6}}, \quad 2$$

The returning sweep in the RDE case should overlap with the forward sweep, since it is a steady-state technique. In practice, however, a small hysteresis is often seen, due to, amongst others, slow electron transfer rates, material depletion and/or capacitance.

3.2 Bulk Electrolysis

A bulk electrolysis (BE) cell consists of a three-electrode setup as do CV and RDE, but with the difference that the solution is stirred, the working electrode has a much larger surface area, and the counter electrode is separated from the bulk solution by a membrane. BE is run either potentiostatically, where the potential is fixed and the current response is measured, or galvanostatically, where the current is fixed, and the potential is instead allowed to vary. Both methods are based on the same chemistry; the bulk of the material in solution gets reduced or oxidized. From the charge passed, the number of electrons involved in the redox process can be calculated, making BE a valuable tool for elucidating the impact of self-association on redox behavior. A typical galvanostatic BE curve is shown in Figure 3-1b, where 80 ml of 50 mM AQDS in 1 M H_2SO_4 is reduced and then oxidized. As material is consumed in the process, a gradually higher overpotential is needed to maintain the current, due to the shifting of the ratio between the oxidized and reduced species, which relates to the reduction potential through the Nernst equation:[81, 83]

$$E_{cell} = E^0 + \frac{RT}{nF}\ln\frac{[Ox]}{[Red]}, \quad 3$$

where [Ox] and [Red] are the concentrations of the oxidized and reduced species respectively.

The perhaps most important piece of information obtained from BE measurements relates to the stability of the material. If the material can be reduced and oxidized through multiple cycles while yielding the same amount of charge every cycle, it can be considered stable, depending on the number of cycles and cycle time.

3.3 Redox Flow Battery Operation

In contrast to the previously presented electrochemical analyses, the redox flow battery is most commonly run in a two-electrode setup. Any potential recorded will therefore be the difference in potential between the oxidation on one half of the cell, and the reduction on the other. In conventional battery characterization, a metric called “C” is commonly used, and 1 C corresponds to charging or discharging the battery in one hour. A charging rate of 2 C then corresponds to 30 minutes before full charge is acquired, and 0.5 C requires two hours. This metric holds little meaning for a redox flow battery as the capacity and power are decoupled. Any given charging rate with the “C” metric could easily be doubled simply by removing half of the reservoir in the tank, while still keeping the current constant.

Instead, the current density in mA cm^{-2} is commonly used, where the area corresponds to the geometric area of the electrodes. The possible amount of current density possible to pull from a redox flow battery is highly dependent on the type and concentration of redox-active material and supporting salt in the electrolytes, the flow rate, and to a lesser degree the thickness and type of the electrodes and membrane. This complicates comparison of the performance

between different reported redox-active molecules, but nonetheless, some metrics are commonly used:[84]

Coulombic Efficiency: The ratio between the discharge capacity and the charge capacity. This is a measurement of how many electrons are "wasted" in unwanted side reactions and numbers exceeding 99.9% are commonly reported.

$$\mathrm{CE}=\frac{Q_{\mathrm{discharge}}}{Q_{\mathrm{charge}}}$$

Voltage Efficiency: The ratio between the voltage during discharge and the voltage during charge. From this number, information on the overpotential required to drive the redox reactions is acquired. The overpotential has three components: the mass transfer resistance, the charge transfer resistance, and ohmic losses. These components play differently large roles in different systems and are more accurately investigated using Electrochemical Impedance Spectroscopy (EIS).[85] The voltage efficiency will decrease sharply when increasing the current density and should be compared at as similar conditions as possible.

$$\mathrm{VE}=\frac{V_{\mathrm{discharge}}}{V_{\mathrm{charge}}}$$

Energy Efficiency: The fraction of the energy spent on charging the battery that can be retained during discharge. In a scientific context, the energy efficiency is simply the product of the voltage efficiency and the coulombic efficiency, in other words:

$$\mathrm{EE}=\mathrm{CE}\cdot\mathrm{VE}$$

This will of course neglect energy losses suffered by potential heating/cooling, pumping and various other parts of electronic equipment included in the complete redox flow battery system. These losses, however, are included in the metric called the *system energy efficiency*, but this is mostly used either in works of highly applied science or in the industrial domain.

Capacity Utilization: The fraction of the theoretical capacity accessed in each cycle. It can either relate to the charge capacity, discharge capacity or the average between them.

$$\mathrm{CU}=\frac{\mathrm{Q_n}}{\mathrm{Q_{theoretical}}}$$

Capacity Retention and Calendar Aging: The difference in accessed capacity between one cycle and another. Providing a high coulombic efficiency, either the charge or discharge capacity can be used, and the average value over the relevant cycles is usually reported. This gives a valuable indication on the electrochemical/chemical stability of the system including the redox-active molecule, electrodes and membrane.

$$\mathrm{CR}=\frac{Q_n}{Q_{n\text{-}1}}$$

However, a flow battery system with either a relatively large membrane and electrode assembly, or relatively small electrolyte reservoirs can cycle a battery many times in a short period of time. Therefore, the capacity retention metric is preferably complemented with a report on the calendar aging:

$$\mathrm{CA}=\frac{Q_0-Q_n}{\mathrm{time}}$$

3.4 Coupled Electron Transfers and Scheme of Squares

The following section covers some of the theory on electron transfers in a mathematically simple manner. The reader is encouraged to consult Bard and Faulkner[81] or Compton and Banks[83] for the mathematical treatment of these concepts.

In the most general redox reaction scheme,

$$\mathrm{Ox} + e^- \rightleftharpoons \mathrm{Red}, \qquad \text{E1}$$

a reactant Ox acquires an electron and is reversibly reduced to a product Red. Depending on the relative energy levels – or potentials – of Ox, e^-, and Red, there will exist one point in this equilibrium that is the most thermodynamically favorable one.[83] Any deviation from this point (which is characterized by the relative concentrations of Ox and Red) will incur a difference in potential between the populations of the reactants and the products, according to Le Chatelier's principle.[83, 86] In response to this, a redox reaction will occur, where electrons flow from the side that has the higher energy to the one with lower energy. In summary, the advance or retreat of E1 is governed by the relative abundances of Ox and Red. This necessitates the electrochemist to take several different scenarios into account, where the concentrations of the reactants and products of a reaction are affected by external processes. The processes acting on the system can be categorized into being either an electron transfer reaction, denoted by the letter E, or a chemical reaction, C. Only a selection of all the possible situations are covered in this section. Simulated CVs of electron transfer reactions of the type "E" and "CE" are shown in Figure 3-2. The CVs have been normalized by the square root of the sweep rate, which in the case of uncoupled electron transfer reactions (type "E") yield identical curves according to Equation 1.

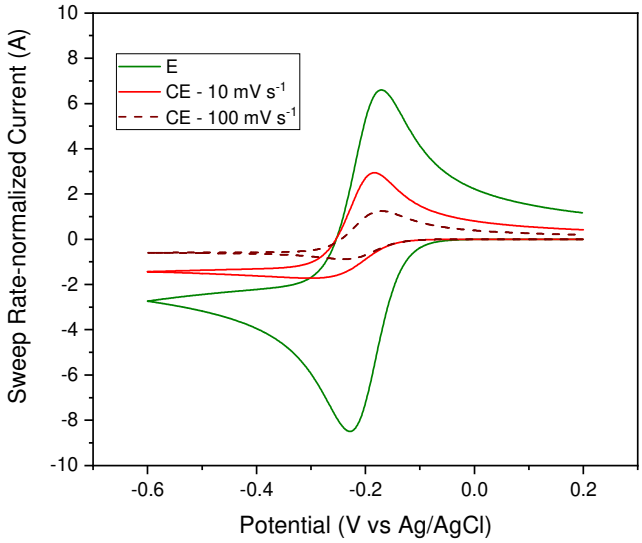

Figure 3-2: Simulated sweep rate-normalized CVs of E (green line) and CE type reactions at two different sweep rates (red and brown dashed lines).

If prior to the above reaction, Ox is generated by a separate chemical reaction:

$Y \rightleftharpoons Ox$ C1

$Ox + e^- \rightleftharpoons Red$ E1

then the coupled reactions are termed to be of a CE type.[81] The amount of redox-accessible material, and thus the current, will depend on the equilibrium constant of the preceding reaction. In a CV, the current response will depend on the sweep rate, as seen by the red and brown lines in Figure 3-2. As material is reduced, the Ox species on the right side of C1 are consumed, and the concentrations of Y and Ox are shifted away from equilibrium. Consequently, more Y is converted to Ox, and at lower sweep rates the reaction is given more time to equilibrate, leading to a higher sweep rate-normalized current.

Similar to the reaction in which Ox is generated, there can exist reactions that instead consume Red, leading to the following scheme, which is termed "EC":

$Ox + e^- \rightleftharpoons Red$ E1

$Red \rightleftharpoons X$ C2

Figure 3-3 shows sweep rate-normalized CVs of an EC reaction at sweep rates of 10, 100 and 500 mV s^{-1}. The current of the oxidative sweep heavily depends on the rate at which Red is consumed in C2, and the sweep rate. The higher the sweep rate, the less time Red is given to convert, and the larger the oxidative current on the returning sweep. If the time of the sweep is very short on the timescale of the chemical reaction, the EC reaction will eventually resemble a simple E reaction.

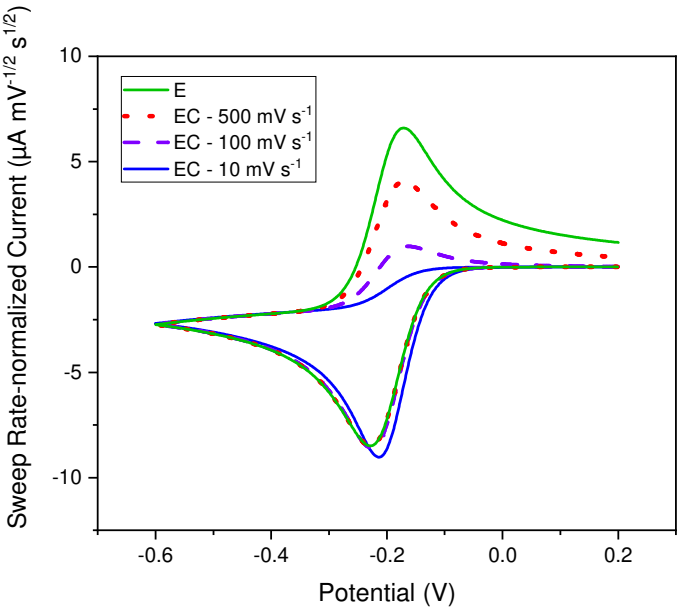

Figure 3-3: Simulated sweep rate-normalized CVs of an EC reaction at three different sweep rates as well as an E reaction for comparison.

Any combination of E and C is possible, and the character convention of E and C gives very compact abbreviations to possibly quite complex reactions. Depending on the pH, the reduction of a quinone can either involve two electrons, two electrons and one proton, or two electrons and two protons, largely determined by the pK_a values of each formed species.[81, 87] As such, taking the order of the electron transfers and chemical reactions into account, nine different combinations are possible, which can be depicted in a model called the *Scheme of Squares,*[88] see Figure 3-4.

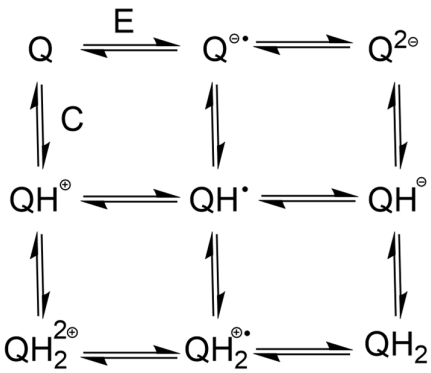

Figure 3-4: A general scheme of squares model for a system of two electron transfers (E) and two chemical reactions (C).

The pathway taken will be decided by the relative rates of the competing reactions between each position, and thus, often not only one path is taken. Furthermore, the path from the starting material to the product is not necessarily the same as the return route.[89]

Although the scheme of squares can be used for any combination of electron transfers and chemical reactions, it is most commonly applied to systems of coupled electron and proton transfers.[87, 89, 90]

The potential for a coupled electron and proton transfer can be calculated using a modified variant of Equation 3. The equilibrium

$$RedH^+ \rightleftharpoons Red + H^+, \qquad C3$$

is recognized, with an equilibrium constant of

$$K_a = \frac{[Red][H^+]}{[RedH^+]}.$$

Substitution into Equation 3 yields

$$E_{cell} = E^0 + \frac{RT}{nF} \ln \frac{[Ox]}{[Red]} = E^0 + \frac{RT}{nF} \ln \frac{[Ox][H^+]}{[RedH^+]K_a}. \qquad 4$$

By separating $[H^+]$ and K_a from the logarithmic term, making a conversion from the natural logarithm to the decadal logarithm, and evaluating R, T and F in those terms, a form of Equation 4 is acquired:

$$E_{cell} = E^0 + \frac{2.303RT}{nF} \log(H^+) - \frac{2.303RT}{nF} \log(K_a) + \frac{RT}{nF} \ln \frac{[Ox]}{[RedH^+]}, \qquad 5$$

$$E_{cell} = E^0 - \frac{0.059}{n} pH + \frac{0.059}{n} pK_a + \frac{RT}{nF} \ln \frac{[Ox]}{[RedH^+]}. \qquad 6$$

3.5 Characterization of NDI Self-Association with ^{1}H-NMR Spectroscopy

If not explicitly referenced otherwise, all of the following theory regarding Nuclear Magnetic Resonance (NMR) spectroscopy, and diffusion NMR is referenced to the comprehensive review article by Price.[91]

NMR is one of the most commonly used tools for chemical characterization, with hydrogen being the atom most commonly utilized. When introducing the most abundant isotope of hydrogen, ^{1}H into an externally applied magnetic field, the nuclear spin can be seen to attain a *precessing* motion about the axis of the magnetic field likewise to the movement created by any spinning mass exposed to a gravitational force, for instance a spinning top. The frequency of the precession is proportional to the strength of the magnetic field. The reason why ^{1}H, together with many other isotopes, precess in a magnetic field is due to their *non-zero magnetic spin moments.* For example, in a magnetic field of 9.6 Tesla, a ^{1}H nucleus will precess with a frequency of approximately 500.13 MHz, which is usually the figure of performance for a given magnet in an NMR system, and not the actual field strength. This frequency is known as the Larmor frequency, ν_0, given by the Larmor equation:

$$\nu_0 = -\frac{\gamma B_0}{2\pi}, \qquad 7$$

where γ is the gyromagnetic ratio and B_0 the magnetic field strength. ^{1}H has a very high gyromagnetic ratio compared to other isotopes, making it sensitive to changes in the magnetic field, and thus popular for use in NMR analysis. When recording a standard liquid-state ^{1}H-NMR spectrum, a sample of molecules containing hydrogen atoms dissolved in a deuterated solvent is inserted into the magnet. The magnetic field, which is generated by a superconductor

kept cool by a jacket of liquid helium, induces precession of the hydrogen nuclei forming an equilibrium state. A short-pulsed current is then passed through a coil surrounding the sample which creates an electromotive force on the nuclei, which in turn will align their magnetic dipole moments away from the NMR magnet's main field. The frequencies at which the nuclei after the pulse relax back to their initial spin alignments can be recorded by the current induced in the sample coil and contains information on the chemical environment of the nuclei.

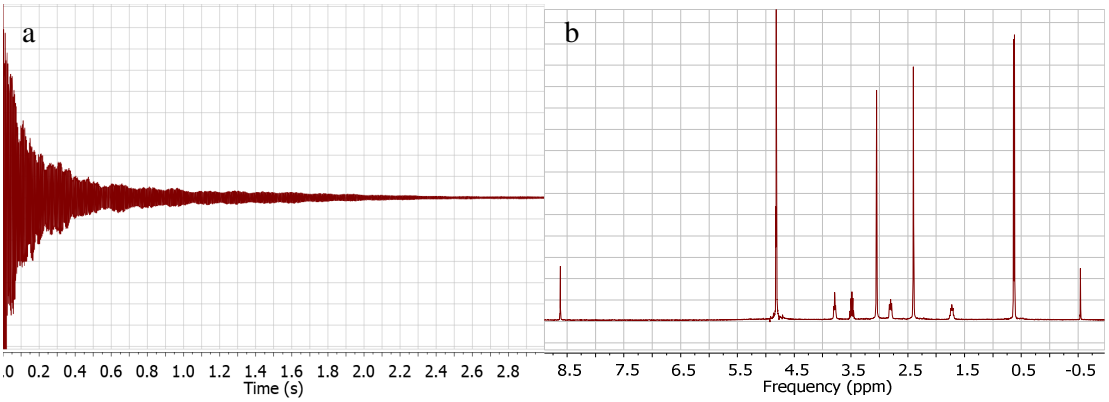

Figure 3-5: ^{1}H-NMR spectra of 2H-NDI in D_2O in the a) time domain (FID) and b) Fourier-transformed into the frequency domain.

The recorded signal, known as the free induction decay (FID), is an oscillating time-dependent data array and provides limited accessibility to information on the system. The FID is therefore processed with a Fourier transform and each chemically inequivalent nucleus is instead resolved on a frequency-dependent spectrum and characterized by its chemical shift in ppm, see Figure 3-5.

In the case of molecular self-association, the chemical environments surrounding the information-carrying protons will vary between a self-associated form, perhaps a dimer, and its chemically isolated, or monomeric, counterpart. If these states do not change faster than the time corresponding to the difference between their relaxation frequencies, two separate peaks will be resolved. However, if the chemical exchange, which is the rate at which the dimer associates and dissociates, is faster than this time, a concentration-dependent displacement of the chemical shift will be observed,[92, 93] and the measured shift will be the average of the separate shifts of the monomer and the dimer,[94] exemplified in Figure 3-6.

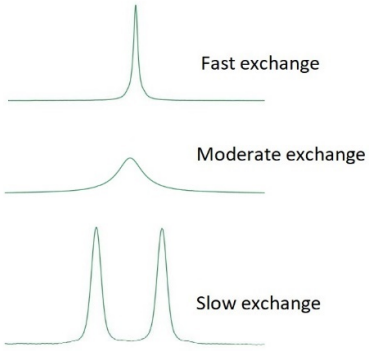

Figure 3-6: A depiction of the influence of chemical exchange on chemical shift and peak shape.

The merged peak, that has a concentration-averaged shift of the individual constituents, can be modelled through the following equations:[53, 95]

Assuming only dimer formation – the dimer model:

$$\delta_{measured}=\delta_m+(\delta_d-\delta_m)\frac{\sqrt{1+8KC_0}-1}{\sqrt{1+8KC_0}+1}, \qquad 8$$

Allowing higher order aggregates – the isodesmic model:

$$\delta_{measured}=\delta_m+\frac{4(\delta_d-\delta_m)KC_0\left(2-\frac{4KC_0}{(1+\sqrt{1+4KC_0})^2}\right)}{\left(1+\sqrt{1+4KC_0}\right)^2}, \qquad 9$$

Where δ is the chemical shift for the respective index, d stands for dimer and m for monomer, K the equilibrium constant, and C_0 the total concentration. Although the three unknowns, δ_m, δ_d and K make an accurate curve fitting problematic, a good approximation of the monomer shift can sometimes be gained by measuring at a sufficiently low concentration.

3.6 Diffusion NMR

In diffusion NMR, the sensitivity of the nucleus to changes in the magnetic field is taken advantage of by the application of a magnetic field gradient. When a gradient is applied, the nuclei located in the stronger part of the field will precess with a higher frequency than those subject to a weaker field. In other words, this allows for spatial labelling of the nuclei based on their *precession* frequencies.

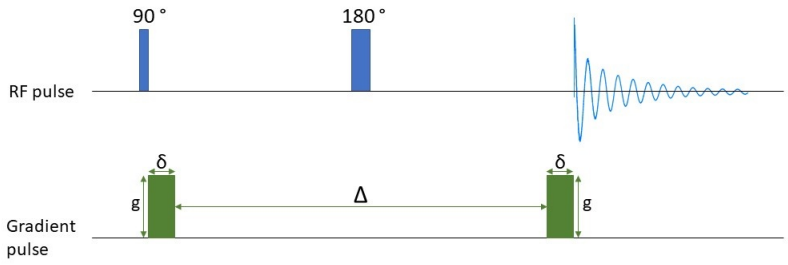

Figure 3-7: A typical pulse field gradient spin echo (PFGSE) pulse sequence.[91]

The basic pulse sequence for measuring the diffusion of molecules in a sample is shown in Figure 3-7, although in practice, the commonly used sequences are more advanced.[91] A radiofrequency pulse (RF) is applied perpendicular to the magnetic field, so that the angle of the precession is shifted 90° away from the z-axis resulting in a xy-component of the precession. A magnetic gradient pulse of a certain strength (g) and duration (δ) is then applied, which allows the nuclei in the sample to be *spatially encoded*. Due to the difference in location of the nuclei, some will precess slightly more slowly than others and vice versa. This is allowed for a time (Δ), during which the molecules self-diffuse. A 180° RF pulse is applied after half of Δ, flipping the spin of the nuclei, putting the more slowly precessing nuclei ahead of those precessing more quickly. In the absence of diffusion, this would lead to all the nuclei regathering after the second gradient pulse, resulting in what is called a spin-echo with a peak intensity of S_0. However, due to the change in location during Δ, due to molecular self-diffusion, the regathering will be incomplete, and the spin-echo will be attenuated. This

attenuated peak height or integral, S, correlates to the diffusion coefficient of the analyte through the following equation:[91]

$$\frac{S}{S_0} = e^{-\gamma^2 \delta^2 g^2 D(\Delta - \frac{\delta}{3})}. \quad 10$$

3.7 Density Functional Theory

This section serves to give a general introduction to DFT as well as a limited display of its uses in applied chemistry.

3.7.1 Quantum Mechanics

The early 1920s was a period of quite rapid development in the field of physics and in particular, quantum mechanics. Based on Einstein's findings on the photoelectric effect,[96, 97] prominent mathematicians and physicists such as Max Planck, Erwin Schrödinger, Werner Heisenberg, and Louis de Broglie amongst many others set out to define a number of quantum mechanical postulates. The first postulate says that the relationship between time and location for any set of particles can be described by a wave function denoted by the letter Ψ. The wave function for a particle holds no information in itself, but its squared value, $|\Psi|^2$, gives the probability of finding the particle as a function of distance from the center. 20 years following Einstein's notion that light could behave as a particle of energy as well as a wave, the famous Schrödinger equation was published.[98, 99] The Schrödinger equation in its time-independent general form,

$$\hat{H}\Psi = E\Psi, \quad 11$$

is used to extract (observe) information about the system described by the wave function. In the above case, $\hat{H}$ is an operator known as the Hamiltonian operator and yields the energy, E, of the system if applied to the wave function. The Schrödinger equation is connected to another quantum mechanical postulate that says that every wave function has observables that are associated with operators.

The Schrödinger equation can only be solved exactly for very simple systems, and the art of applying quantum mechanics to practical applications is to know which approximations are appropriate for a certain application.

3.7.2 Quantum Chemistry

In quantum chemistry, fundamental quantum mechanical principals are used to obtain information about chemical systems. In the case of investigating the energy of a molecule, the wave function for the molecule is typically approximated by a linear combination (addition) of a number N of atomic orbitals φ, also known as basis functions which together make up a basis set:

$$\Psi = \sum_{i=1}^{N} c_i \varphi_i. \quad 12$$

The principle behind this method is that the energy acquired from observing the system with the Hamiltonian operator will always be higher than the actual energy of the system. In this way, the weighing factors, c_i, are varied to minimize the observed energy of the system and thereby improving the approximation. The method is called the variational method or self-consistent field theory and saw much development in the years 1928-1930 by Douglas Hartree,[100] John Clark Slater,[101] and Vladimir Fock[102] amongst others. This method, however,

did not see much use until the advent of the computer, which was technologically mature enough to handle quantum chemical calculations only decades later.

3.7.3 Density Functional Theory

The atomic orbitals used in the approximation can in turn be approximated in many different ways, such as by Slater-type orbitals, Gaussian-type orbitals or combinations of the both. However, instead of approximating the atomic orbitals explicitly which is quite computationally demanding, expressions of electron density ρ can be used instead. In this approach, the energy for the system is given by the Kohn-Sham equations presented by Walter Kohn and Lu Jeu Sham in 1965:[103]

$$E(\rho)=T_e(\rho)+V_{ne}(\rho)+V_{ee}(\rho)+\Delta T(\rho)+\Delta V_{ee}(\rho), \qquad 13$$

Each component of this function of ρ is also a function of ρ which makes it a functional, or a function of a function. T_e is the kinetic energy of the electrons that do not interact with each other. V_{ne} is the potential energy that arises from interactions between nuclei and electrons and V_{ee} due to the repulsion between electrons. The two final terms are corrections to the kinetic and potential energies of the electrons. The energy contribution of these terms is called the exchange-correlation (XC) energy and the choice of XC functional used to describe this is of major importance to the accuracy of the method. The XC functional is not an exact formulation, and as a consequence, DFT cannot use the variational method in the same way as is done in other quantum chemical analysis methods.

Most DFT-calculations are run using commercial software such as *Gaussian*, *VASP* or *Schrodinger's Jaguar* where a molecular structure is input as a list of atoms with coordinates. An XC functional is chosen together with a basis set, and a commando to optimize the geometry of the input structure is given. The software iteratively minimizes the energy of the system and an optimized structure is acquired with an accompanying energy value. The energy value can then be used to calculate various thermodynamic properties such as reduction potentials, pK_a values and reaction heats, of which the former two applications will be used in this thesis.

4 Results and Discussion

In the present work, the electrochemistry of the five organic molecules listed below was investigated experimentally, out of which BTMAP-Fc was only used in the positive electrolyte for redox flow battery testing, and was not studied on a fundamental level.

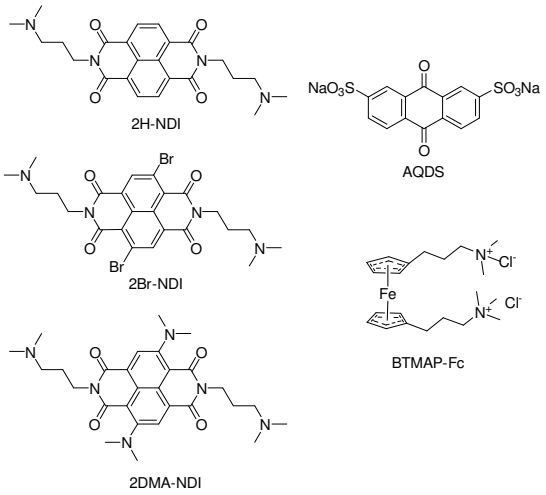

Figure 4-1: Experimentally investigated organic molecules.

4.1 Electrochemical Evaluation of NDIs at Low Concentration

The mechanistic electrochemistry of the NDIs at a low concentration was investigated using CV, ^{1}H-NMR and DFT.

4.1.1 Experimental Cyclic Voltammetry

CVs of 2H-NDI, 2Br-NDI, and 2DMA-NDI at a concentration of 1 mM were recorded in aqueous solution at varying pHs. In Figure 4-2a, CVs of 2H-NDI are shown at pH values ranging between 0 and 7. The system was not examined in alkaline solutions, as the dimethylamine sidechain is deprotonated at higher pH values, turning the molecule insoluble in water. Furthermore, the imide of 2H-NDI has been shown to be reversibly hydrolyzed by hydroxide nucleophilic attack at pH above 8.[104]

Starting at low pH, the first and the second electron transfers have almost the same reduction potential, see Figure 4-2. As the pH increases, the potential for the first electron transfer stays at -0.28 V vs Ag/AgCl, while the second moves toward more negative potentials, see Figure 4-2b. At pH values exceeding 4, the second redox couple has reached its terminal potential of -0.63 V vs Ag/AgCl. The dashed line shows the thermodynamic potential for the unwanted HER (see Section 2.4.1). HER is kinetically slow, however, and can usually be exceeded by a few hundred millivolts before the negative effects become too big.[105] At pH 0, both the first

and the second electron transfers are at most 100 mV more negative than the HER, which should be within acceptable limits for successful flow battery application.

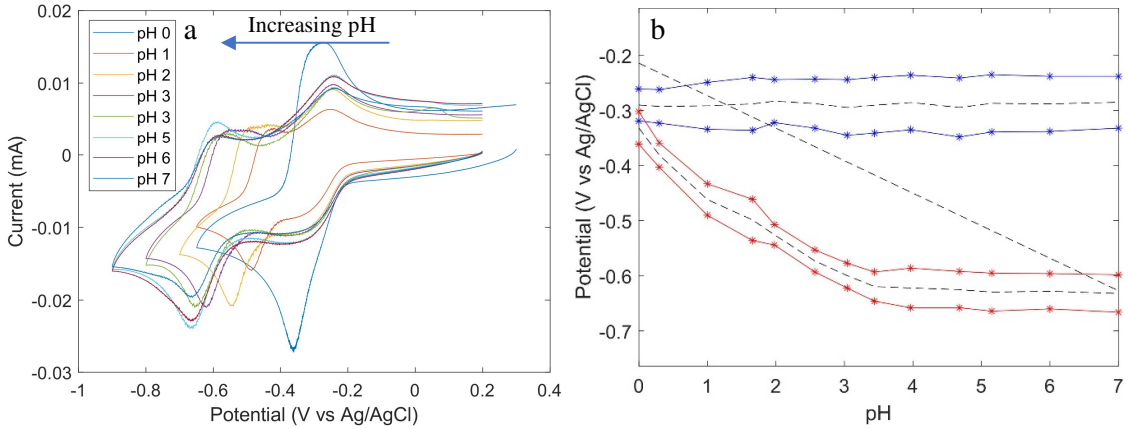

Figure 4-2: Results from pH-dependent cyclic voltammetry of 2H-NDI. a) CVs at pH 0-7 and b) potential-pH dependence. The blue and red markers depict the anodic and cathodic peak potentials for the first and the second electron transfer respectively. The diagonal dashed line shows the thermodynamic potential for the HER. (Paper III)

When increasing the pH, the potential for the second electron transfer travels toward more negative values faster than the potential for the HER, which has a potential-pH slope of -0.059 V per pH unit. The value of the slope for 2H-NDI corresponds to the number of protons and electrons involved in the coupled electron transfer. Figure 4-2b shows a higher slope than -0.059 V per pH at low pH, and this indicates that one electron is coupled to more than one proton, as can be deduced from Equation 6. Therefore, at pH approximately between 1 and 4, the potential for the second electron transfer is 200 to 250 mV more negative than that of the HER, which may be problematic. At neutral pH, which is often preferred AORFBs as it allows the use of cheaper materials for the tanks and other components, the potential for the HER has caught up to that of the second electron transfer, and the parasitic reaction should not occur during cycling.

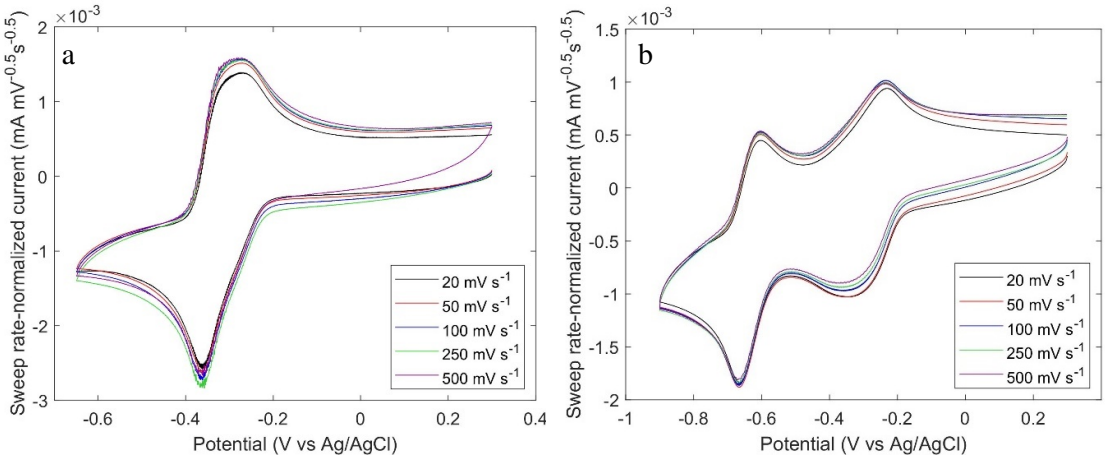

Figure 4-3: Sweep rate-normalized CVs for 2H-NDI at a) pH 0 and b) pH 7. (Paper II)

Figure 4-3 shows sweep-rate normalized CVs for 2H-NDI at pH 0 and pH 7. The shapes and the peak currents align well, indicating chemical stability on the CV timescale as well as electrochemical reversibility. The broadness of the first redox couple at neutral pH may be the juxtaposition of two or multiple redox processes at similar potentials to the nominal reduction. If 2H-NDI forms dimers or other complexes that have reduction potentials slightly different from that of the monomer, such a peak-broadening could be expected.

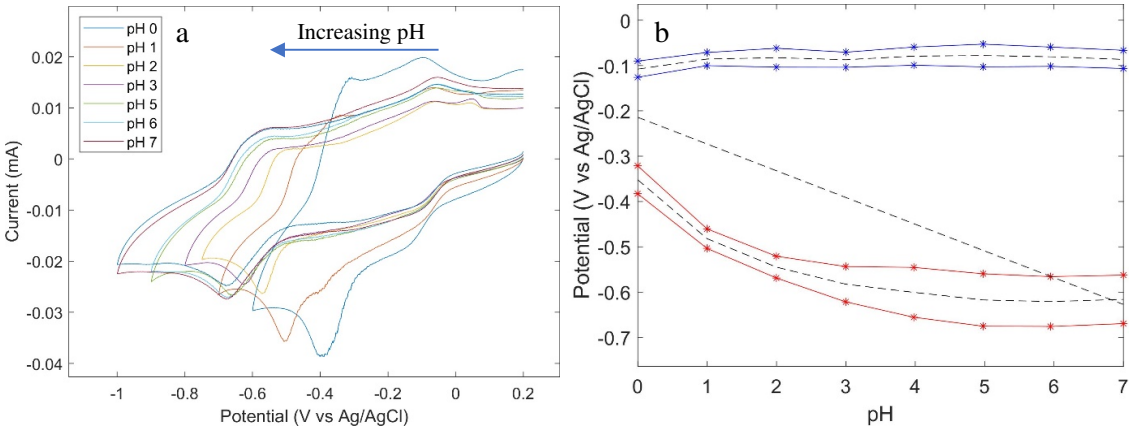

Figure 4-4: Results from pH-dependent cyclic voltammetry of 2Br-NDI. a) CVs at pH 0-7 and b) potential-pH dependence. The blue and red markers depict the anodic and cathodic peak potentials for the first and the second electron transfer respectively. The diagonal dashed line shows the thermodynamic potential for the HER. (Paper III)

Figure 4-4 shows the corresponding results for 2Br-NDI, which is seen to behave similarly to 2H-NDI with only subtle differences in potential. The first redox couple has a potential of approximately -0.1 V vs Ag/AgCl – slightly more positive than that of 2H-NDI – while the potential of the second redox couple matches that of 2H-NDI. However, looking at the sweep rate-normalized CVs in Figure 4-5, the electrochemical behavior of 2Br-NDI departs from that of 2H-NDI. At pH 0, the oxidative peak of the first redox couple decreases slightly with increasing sweep rate, while at pH 7, larger currents at higher sweep rates are seen throughout. These deviations imply chemical reactions coupled with the electron transfers, see Section 3.4.

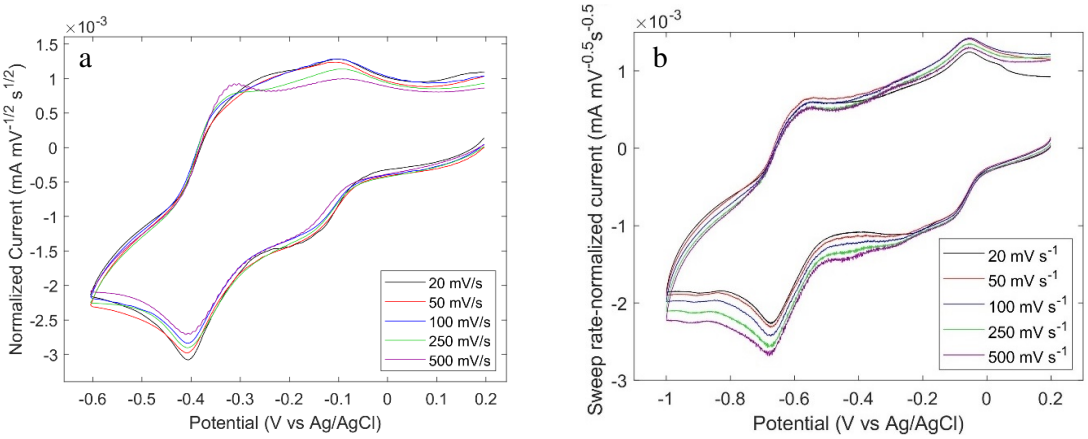

Figure 4-5: Sweep rate-normalized CVs for 2Br-NDI at a) pH 0 and b) pH 7.

Any molecule that degrades on the CV timescale will show a more ideal-looking CV at higher sweep rates, simply because it is given less time to decompose before in this case being oxidized back to the relatively stable starting material. Therefore, it would be instructive to look at the relative size of the anodic and cathodic peak currents, but since the current following the first electron transfer does not clearly decrease but rather reaches a plateau, accurate determination of the peak current for the second reduction is complicated, if not impossible.

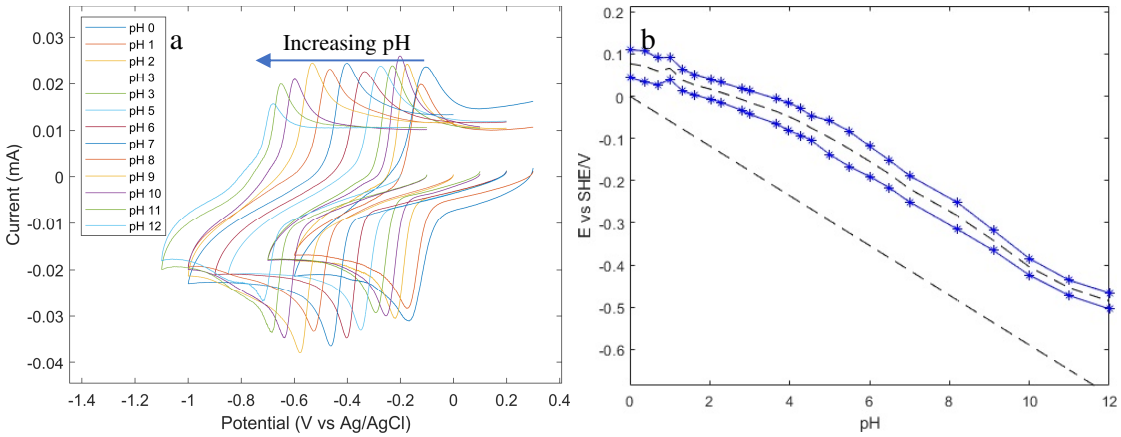

Figure 4-6: Results from pH-dependent cyclic voltammetry of 2DMA-NDI. a) CVs at pH 0-12 and b) potential-pH dependence. The blue markers depict the anodic and cathodic peak potentials, and the diagonal dashed line shows the thermodynamic potential for the HER. (Paper III)

For 2DMA-NDI, the electrochemical behavior differs significantly from those of 2H-NDI and 2Br-NDI, see Figure 4-6. Only one peak can be seen throughout the larger investigated pH range of 0 to 12,[1] which lacks the shapelessness shared by both of the redox couples of 2H-NDI and 2Br-NDI. At low pH, the potential does not change drastically when increasing the pH, and this behavior remains until approximately pH 4, after which the potential-pH dependence increases, to seemingly drop off again at pH values exceeding 11. The increasing pH dependence at increasing pH might make little sense at first sight. Intuitively, if there are fewer protons in the solution, there should be fewer protons involved in the electron transfer.

One clue to the reason behind this reversed relation was given by the color of the solution. At pH 0, the 1 mM electrolyte was bright reddish pink, turned purple at pH 3 and blue at pH 4 and above. While the two dimethylamine groups on the core could be protonated, their pK_a values still needed to be determined, and this was investigated further using ^{1}H-NMR spectroscopy at varying pH values. About 40 NMR samples at solutions between pH 0 and 12 were prepared containing 0.5 mM 2DMA-NDI in 90%/10% H_2O/D_2O together with a 0.2 mM of an NMR reference (3-(Trimethylsilyl)propionic-2,2,3,3-d4 acid) and 2 mM each of tris, imidazole and formic acid in some, and piperazine in others. The last four substances were added as pH indicators in order to get more accurate values on the pH than could be given by the pH meter.

[1] The reason why 2DMA-NDI could be investigated at higher pH values was twofold. Firstly, it retained sufficient solubility even when deprotonated to record CVs at 1 mM, and secondly it did not as easily hydrolyze due to nucleophilic attack by hydroxide molecules as 2H-NDI (and likely 2Br-NDI), supposedly due to the increased electron density on the aromatic core induced by the dimethylamine groups.

Figure 4-7a shows the chemical shifts for the protons on the aromatic core and the dimethylamine and Figure 4-7b on the dimethylamine sidechain. For 2DMA-NDI, the chemical shifts increased upon protonation and the data could be fitted to the Henderson Hasselbalch equation to yield pK_a values for the two protonation equilibria.[106] The dimethylamine on the core was seen to have a pK_a of 3.95 and the one on the sidechain a pK_a of 9.15. Only one of the core dimethylamine groups could be protonated, likely because the decreased electron density in the aromatic core from protonating the first makes the second one too acidic to protonate in aqueous solution.

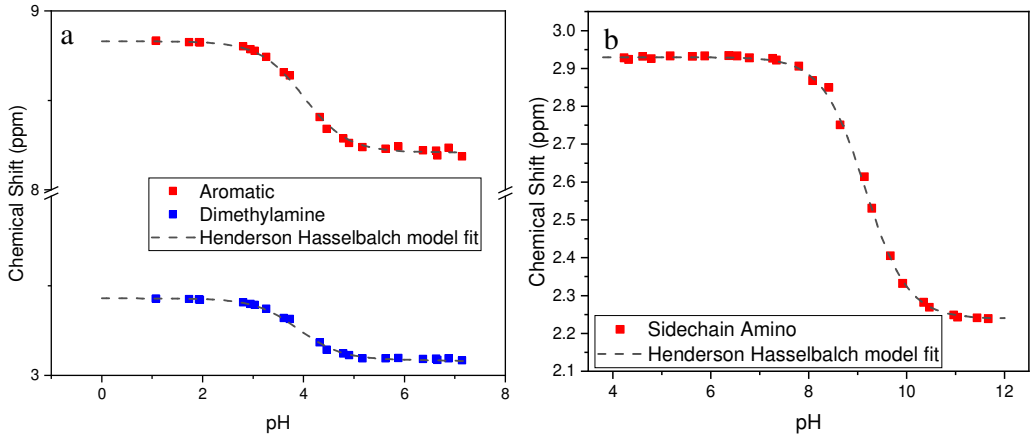

Figure 4-7: ^{1}H-NMR shifts and Henderson Hasselbalch fits of protons on the a) aromatic core and core dimethylamine groups and b) sidechain dimethylamine groups of 2DMA-NDI. (Paper III)

The trend of having a stronger potential-pH dependence at higher pH is thus attributed to the core-protonated version of 2DMA-NDI occurring at lower pH values, and the non-core-protonated version at higher pH values. This will be examined more closely in the following two sections.

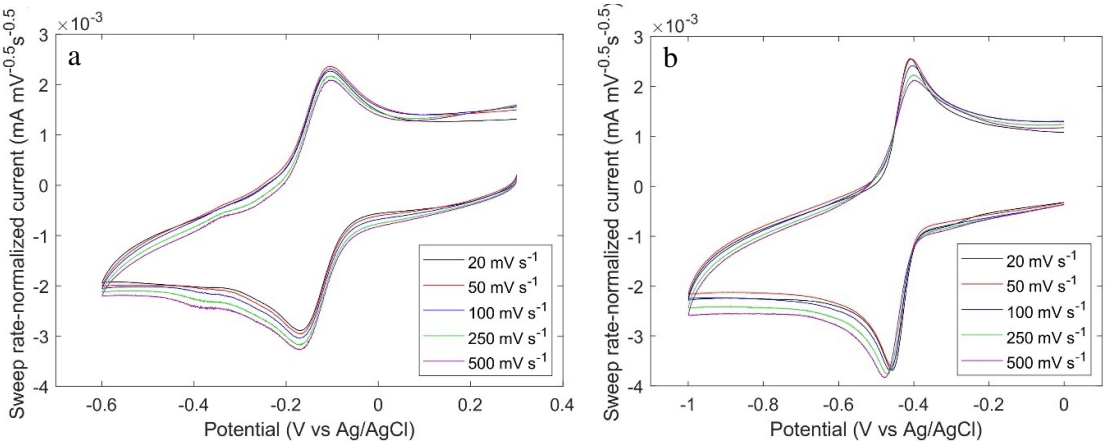

Figure 4-8: Sweep rate-normalized CVs for 2DMA-NDI at a) pH 0 and b) pH 7.

Looking at the sweep rate dependence of 2DMA at pH 0 in Figure 4-8, an indication of good chemical and electrochemical reversibility is given. However, at pH 7, the potential of the cathodic peak moves toward more negative values at higher sweep rates, which might be due to a decreased apparent rate constant at neutral compared to acidic pH.

4.1.2 Scheme of Squares and Computational Electrochemistry

As discussed in Section 3.4, the scheme of squares model can be used to understand the mechanism of coupled electron transfer reactions at different pH values and potentials. In the present section, the nine 2X-NDI species presented in the beginning of the thesis are studied with DFT and CV simulations.

For 2X-NDI, the scheme of squares is shown in Figure 4-9 where E_i corresponds to an electron transfer and C_j corresponds to a protonation step.

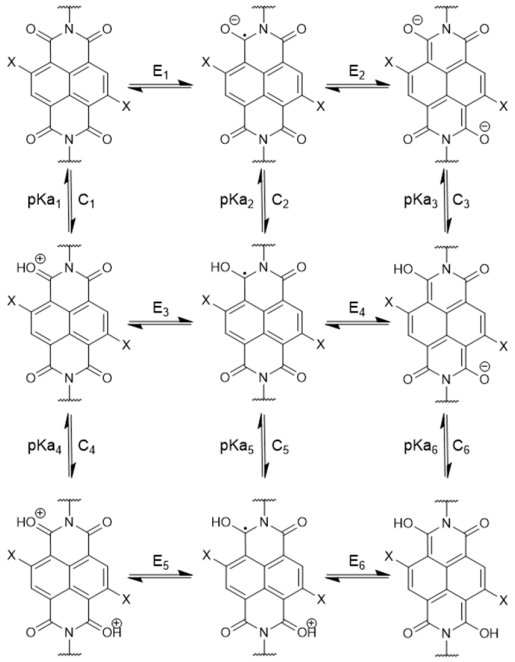

Figure 4-9: Scheme of squares system for 2X-NDI. (Paper III)

The following parameters for the scheme of squares were acquired using DFT calculations:

Table 4-1: Reduction potentials and pK_a values for the scheme of squares system for 2X-NDI. (Paper III)

Substituent X	E_1	E_2	E_3	E_4	E_5	E_6	pK_{a1}	pK_{a2}	pK_{a3}	pK_{a4}	pK_{a5}	pK_{a6}
H	-0.20	-0.58	0.39	-0.09	0.87	0.48	-15.48	-5.44	2.90	-17.28	-9.21	0.45
Br	-0.04	-0.48	0.54	0.02	1.09	0.55	-16.16	-6.47	1.98	-19.62	-10.30	-1.28
F	-0.05	-0.49	0.53	0.01	0.98	0.56	-16.60	-6.73	1.78	-18.01	-10.48	-1.25
CN	0.31	-0.15	0.77	0.38	1.27	0.83	-17.24	-9.62	-0.55	-19.86	-11.31	-3.84
OH	-0.19	-0.59	0.36	-0.09	0.75	0.41	-15.95	-6.72	1.85	-17.16	-10.50	-2.14
NH_2	-0.60	-0.90	-0.23	-0.38	0.48	-0.10	-7.27	-0.93	7.70	-13.71	-1.77	3.07
NH_2-H^+	-0.12	-0.54	0.34	-0.08	0.91	0.29	-13.72	-5.93	1.92	-17.64	-8.07	-1.87
NH_2-$2H^+$	0.35	-0.08	0.91	0.46	1.40	1.01	-19.78	-10.38	-1.28	-23.48	-15.12	-5.79
DMA	-0.55	-0.74	0.02	-0.29	0.45	0.23	-13.48	-3.89	3.68	-14.73	-7.44	1.50
DMA-H^+	-0.13	-0.47	0.27	-0.03	0.81	0.38	-12.82	-6.05	1.51	-19.19	-10.12	-3.22
DMA-$2H^+$	0.35	-0.11	0.95	0.38	1.39	0.88	-20.60	-10.36	-2.07	-21.98	-14.68	-6.14
NO_2	0.34	-0.04	0.90	0.51	1.32	1.13	-19.60	-10.50	-1.90	-20.38	-13.29	-2.88
OMe	-0.15	-0.60	0.39	-0.26	0.70	0.34	-11.95	-2.73	3.00	-15.74	-10.42	-0.35

With the system in Figure 4-9 and the parameters in Table 4-1, some insight on the electrochemistry of the 2X-NDI molecules is provided. As the core-aminated molecules present a more complicated case due to the possibility to protonate the core amines, they are handled separately.

For the remaining species, due to the highly negative values of pK_{a1} and pK_{a4}, all molecules in their oxidized states are unprotonated on their imide oxygen atoms and any reduction must therefore start with a potential of E_1. After the first reduction, the molecule can either be protonated according to C_2 with a $pK_a = pK_{a2}$ or reduced at a potential of E_2. Table 4-1 shows that pK_{a2} is quite negative for all the investigated species, meaning that the protonated radical, 2X-NDIH$^\bullet$, is likely never observed and that the E_2 reduction is chosen, provided that the applied potential is negative enough. After the second reduction, the formed dianion, 2X-NDI^{2-}, can be protonated either once, if pH is below pK_{a3}, or twice if it is below pK_{a6}. If a protonation following the reduction is energetically favorable, then it might proceed concerted together with, or simply very shortly after the electron transfer, and the observed potential can in this case be calculated using Equation 6.

To complement the above qualitative reasoning, CVs and surface concentration profiles (at the electrode surface) were simulated using the DigiElch software suite. The simulated CVs and surface concentrations are presented in the Supplementary Information of Paper III, and were used to produce Table 4-2 in which the scheme of squares pathways for the non-aminated 2X-NDI at various pH values are presented.

Table 4-2: The reductive and oxidative pathways for the non-core-aminated 2X-NDI species at various pH. (Paper III)

Substituent	pH 0	pH 3	pH≥7
H	$E_1E_2C_3C_6/C_6C_3E_2E_1$	$E_1E_2C_3/C_3E_2E_1$	E_1E_2/E_2E_1
Br	$E_1E_2C_3/C_3E_2E_1$	E_1E_2/E_2E_1	E_1E_2/E_2E_1
F	$E_1E_2C_3/C_3E_2E_1$	E_1E_2/E_2E_1	E_1E_2/E_2E_1
CN	E_1E_2/E_2E_1	E_1E_2/E_2E_1	E_1E_2/E_2E_1
OH	$E_1E_2C_3/C_3E_2E_1$	E_1E_2/E_2E_1	E_1E_2/E_2E_1
NO_2	E_1E_2/E_2E_1	E_1E_2/E_2E_1	E_1E_2/E_2E_1
OMe	$E_1E_2C_3/C_3E_2E_1$	$E_1E_2C_3/C_3E_2E_1$	E_1E_2/E_2E_1

The experimental results for 2H-NDI and 2Br-NDI could be better understood after this computational electrochemical analysis. The steeper pH-dependence for the second electron of 2H-NDI at low pH than at intermediate pH was seen to be a result of it coupling with two protons at pH 0, which is lower than pK_{a6}, but only one at pH 3 and eventually none for both 2Br-NDI and 2H-NDI when pH exceeds pK_{a3}.

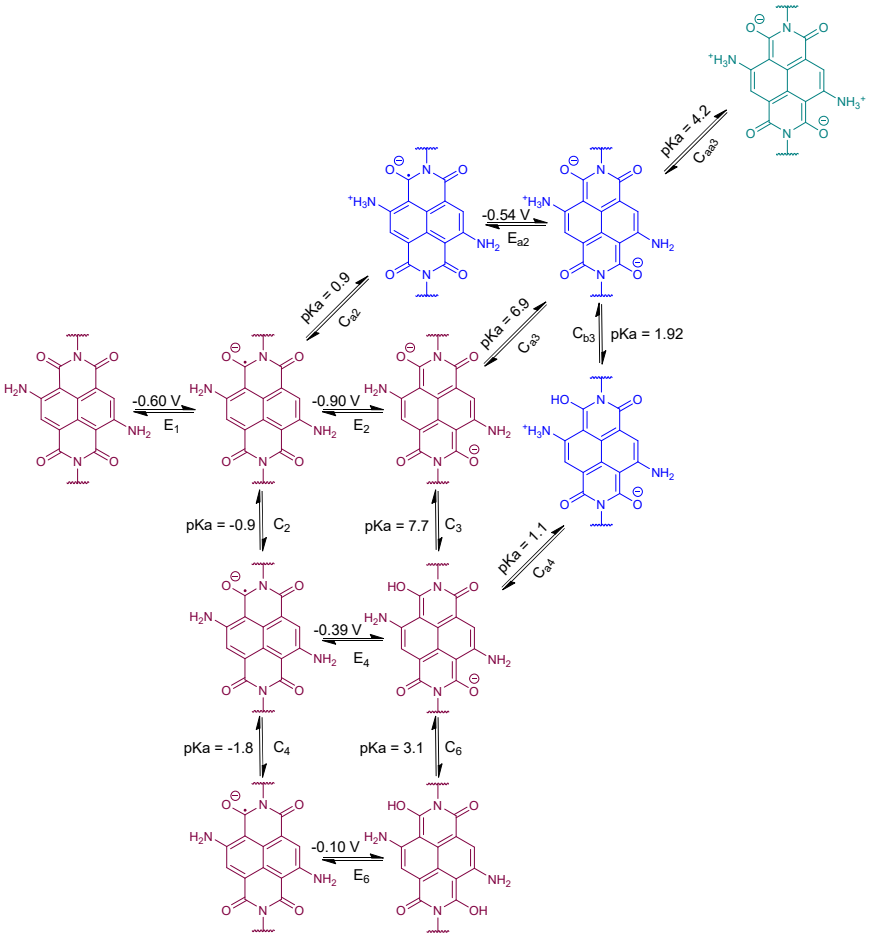

Figure 4-10: Scheme of squares for $2NH_2$-NDI. (Paper III)

In the case of the core-aminated molecules, an extra dimension to the scheme of squares is added for each core-protonation step, adding to the complexity of the system. However, many

structures in this 3x3x3 component matrix are energetically unfavorable and can be disregarded. Thus, abridged square schemes were used for simulating the CVs of $2NH_2$-NDI and 2DMA-NDI, see Figure 4-10 and Figure 4-11. In the schemes, any structure generated by a protonation with a pK_a-value below -2 was considered too unfavorable to be included in the simulations. Apart from this, some additional reactions were removed based on similar reasoning, as well as simply on the empirical observation that they had no impact on the simulated results.

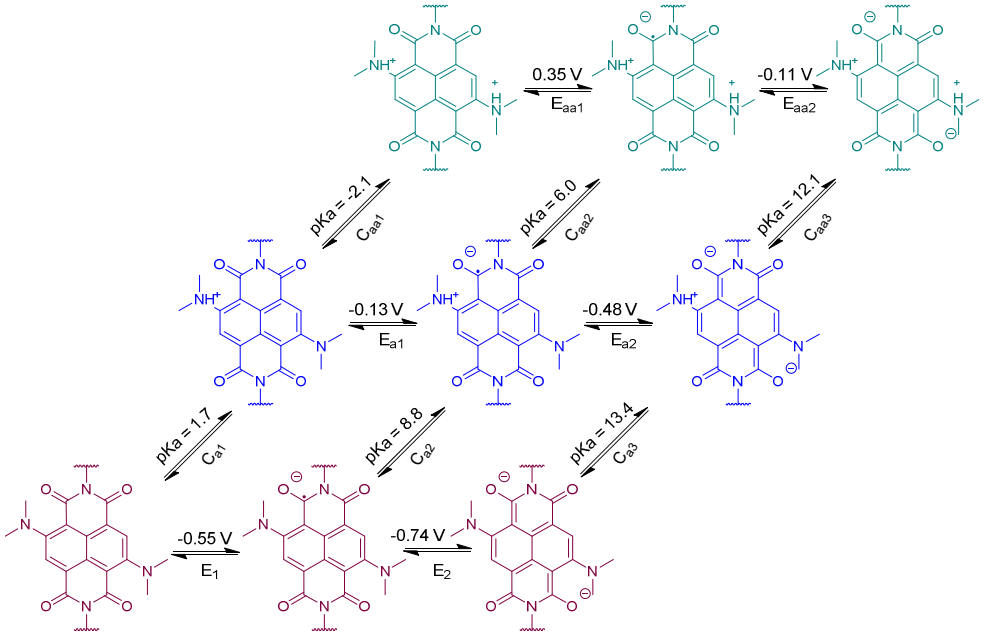

Figure 4-11: Scheme of squares for 2DMA-NDI. (Paper III)

The simulated CVs in the pH ranges that were deemed relevant are shown in Figure 4-12 and the potential-pH dependencies in Figure 4-13.

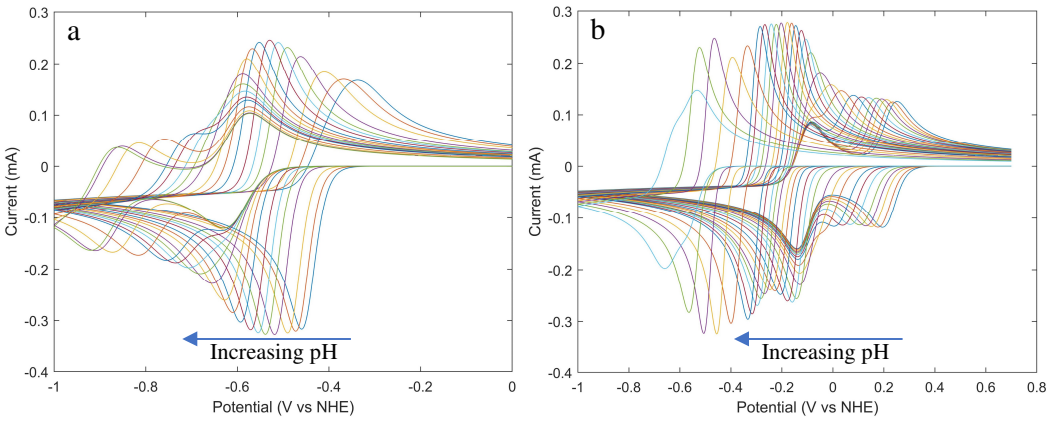

Figure 4-12: CVs of a) $2NH_2$-NDI and b) 2DMA-NDI at pH 0-9 and 0-12 respectively. (Paper III)

At low pH, $2NH_2$-NDI only has one redox couple with a potential that decreases with increasing pH. The pH-dependence is a result of the pK_a of the core-amines increasing between 5 and 8 units when an electron is added to the aromatic system, and as a consequence, one of the core-

amines is immediately protonated following the first reduction. This also explains why the simulated potential for the reduction is more positive than E_1. Further, the reduction potential for the core-protonated radical anion is more positive than that of the starting material, and therefore, this trend is seen at pH values significantly beyond the pK_a of C_{a2} in Figure 4-10a.

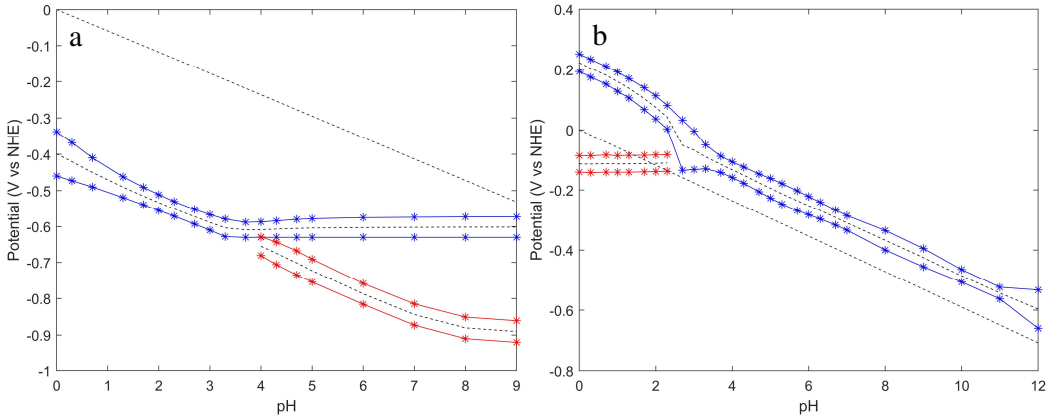

Figure 4-13: Potential – pH dependence on simulated CVs for a) $2NH_2$-NDI and b) 2DMA-NDI. The blue and red markers depict the anodic and cathodic peak potentials for the first and the second electron transfer respectively, and the dashed lines show the thermodynamic potential for the HER. (Paper III)

The surface concentration profile in Figure 4-14a shows that roughly 70% of the reduced $2NH_2$-NDI molecules exist in a di-protonated form with the protons on the core amines, and 30% with the protons on the oxygen atoms, corresponding to the $E_1C_2E_4C_6$ and $E_1C_{a2}E_{a2}C_{b3}C_{a4}C_6$ pathways respectively. At about pH 3, the potential of first electron levels out at E_1 which is -0.6 V vs NHE, and the population of doubly reduced molecules starts containing some mono-protonated species. At pH 7, the $E_1E_2C_3$ pathway dominates, and at pH 9, E_1E_2 dominates.

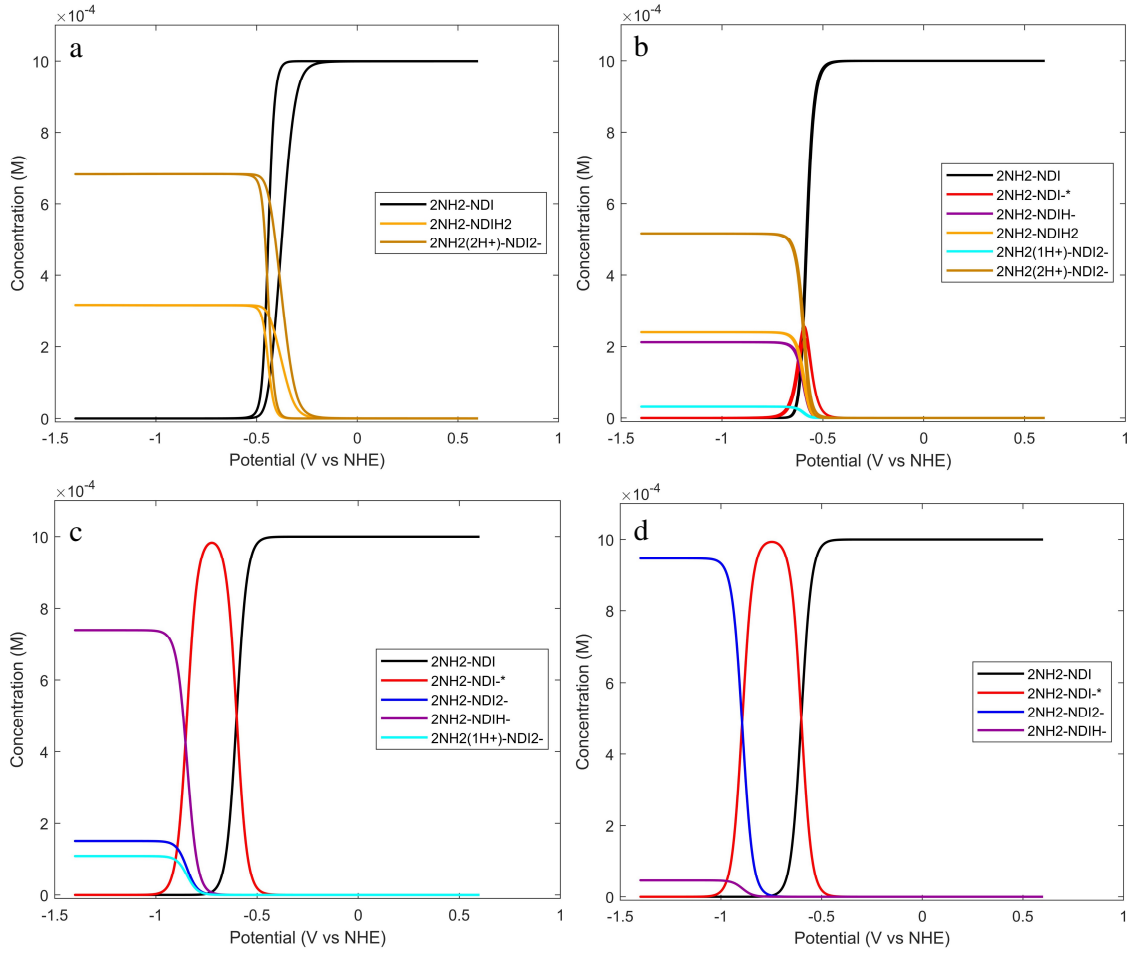

Figure 4-14: Surface concentrations for 2NH$_2$-NDI in a) pH 0, b) pH 3 and c) pH 7 and d) pH 9. (Paper III)

2DMA-NDI has, in contrast to 2NH$_2$-NDI, two redox couples at low pH and one only at higher pH values. Similar to what was seen experimentally, the starting material at pH 0 is the mono-core-protonated species whose first reduction is coupled with a proton according to $E_{a1}C_{aa2}$ and the second reduction simply takes the E_{aa2} path. At pH 3 and above, the potential for the $E_{a1}C_{aa2}$ path becomes more negative than E_{aa2} and only one peak is seen for the two electrons. Upon increasing the pH, the protonated starting material is replaced for its unprotonated analogue, and the di-protonated radical anion is only seen at a decreased concentration at pH 3, and is too short-lived to be seen above pH 7, as shown in Figure 4-15. The concerted E_1C_{a2} path has a much more positive reduction potential at pH 0 of -0.03 V than both E_1 at -0.55 V and E_{a1} of -0.13 V and even the concerted $E_{a1}C_{a1}$ reaction which has a potential of -0.05 V. Therefore, when pH increases sufficiently far above the pK_a of C_{a1} that the $E_{a1}C_{aa2}$ will not occur, the E_1C_{a2} path will be preferred for the first electron. The second electron will be transferred coupled with a proton either along $C_{aa2}E_{aa2}$ or $E_{a2}C_{aa3}$ which both will occur at a potential of 0.24-0.059·pH V vs NHE.

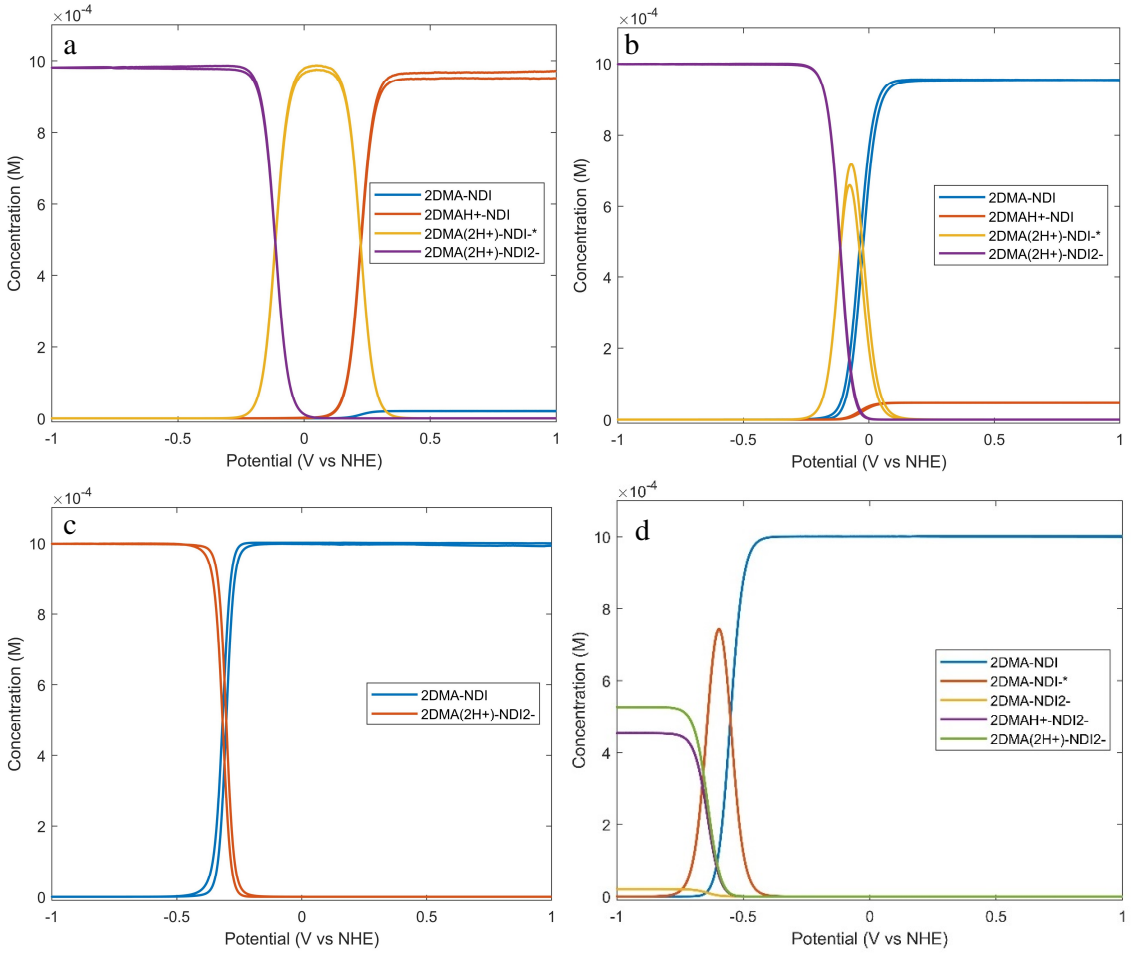

Figure 4-15: Surface concentrations of 2DMA at a) pH 0, b) pH 3, c) pH 7 and d) pH 12. (Paper III)

Eventually, at high pH, the E_1 will proceed uncoupled with protons and two peaks will be emerge from the single one. This behavior, however, will likely be of little practical consequence as, experimentally, 2DMA-NDI is only stable for minutes at pH 12 before turning first green and then yellow in solution.

A collection of the calculated reduction potentials for the studied 2X-NDI species at pH 0 and pH 7 are given in Table 3. The reduction potential of a redox flow battery candidate needs to be as negative as possible, in order to provide a high voltage in a battery, but still not so negative that the HER comes into play. The thermodynamic reduction potential for the HER is by definition 0 V vs SHE, but can be surpassed slightly, as shown in Figure 2-3.

Table 3: Calculated reduction potentials at pH 0 and pH 7 for 2X-NDI. (Paper III)

	E vs SHE (V) - pH 0			E vs SHE (V) - pH 7		
X	1st e-	2nd e-	Average	1st e-	2nd e-	Average
H	-0.20	-0.38	-0.29	*-0.20*	*-0.58*	-0.39
Br	-0.04	-0.36	-0.20	-0.04	-0.48	-0.26
F	-0.05	-0.38	-0.22	-0.05	-0.49	-0.27
CN	0.31	-0.15	0.08	0.31	-0.15	0.08
OH	-0.19	-0.48	-0.33	-0.19	-0.59	-0.39
NO_2	0.36	0.01	0.18	0.34	-0.04	0.15
OMe	-0.16	-0.41	-0.28	-0.15	-0.60	-0.38
$2NH_2$-NDI	-0.40	-0.40	-0.40	-0.60	-0.84	-0.72
2DMA-NDI	0.22	-0.11	0.05	-0.31	-0.31	-0.31

The calculated reduction potentials for 2H-NDI and 2Br-NDI were underestimated by between 120-200 mV compared to the experimental values, while the reduction for 2DMA-NDI was underestimated only by between 27-90 mV, depending on the pH. The non-core-aminated species all have two redox couples, and the average is therefore used as a metric for comparison. Taking all of this into account, at pH 0, 2H-NDI, 2OH-NDI, 2OMe-NDI and $2NH_2$-NDI are identified as interesting candidates for redox flow battery application. At increasing the pH to 7, the potential of 2DMA-NDI decreases relative to the HER, showing promise as well.

4.2 Self-association of Organic Molecules in Aqueous Solution

The self-association of 2H-NDI and AQDS was studied with a combination of conventional chemical analysis, using NMR spectroscopy and diffusion NMR, and electrochemistry, using cyclic voltammetry and rotating disk electrode voltammetry. Organic molecules can form complexes bound by non-covalent interactions either into dimers or higher order complexes according to an isodesmic model.[93]

4.2.1 Concentration-dependent ^{1}H-NMR Spectroscopy

The treatment in Section 3.5 to gauge the self-association of an organic molecule was done on AQDS in a groundbreaking article that simultaneously showed that this self-association severely hampered redox flow battery performance.[53] This method was used on 2H-NDI in neutral buffered aqueous solution, and the proton on the aromatic naphthalene core was seen to shift in position and increase in broadness upon increasing the concentration, see Figure 4-16. The chemical shifts were fitted to the dimer and isodesmic models in Equations 8 and 9 to yield equilibrium constants of 146 M^{-1} for the dimer model and 104 M^{-1} for the isodesmic model.

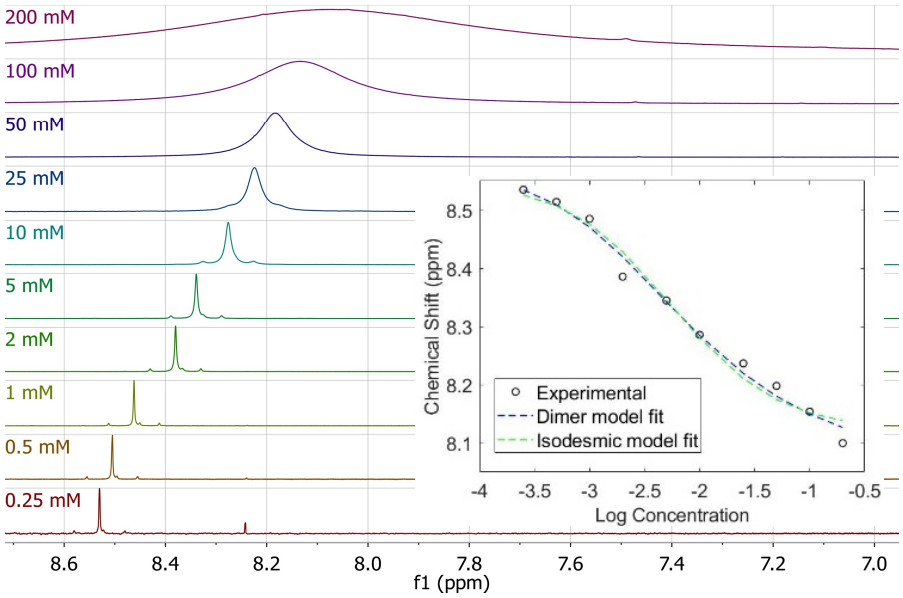

Figure 4-16: Chemical shift of the aromatic proton of 2H-NDI in pH 7 0.5 M sodium phosphate buffer in D_2O. The fittings of the chemical shifts to a dimer and isodesmic model are shown in the inset. (Paper II)

These values of 2H-NDI are significantly higher than those reported for AQDS,[52] which were in the order of 8 M^{-1}.

A distinction between the various complexes was considered out of the scope of this thesis, and for simplicity, dimer formation is assumed in the following discussion although higher order aggregation is possible. The equilibrium constants can be used to calculate the fraction of monomer occurring in solution.

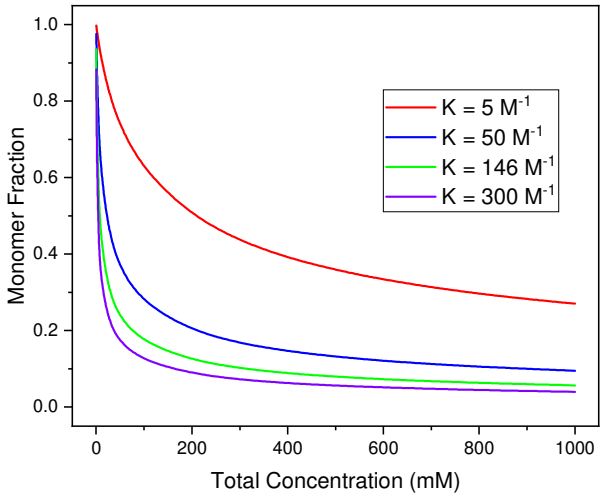

Figure 4-17: Monomer fractions for different equilibrium constants.

As can be seen in Figure 4-17, for a relatively low equilibrium constant of 5 M^{-1}, most of the species in solution exist as dimers at a concentration of 0.5 M, and only 27% are monomeric at 1 M. A tenfold increase to 50 M^{-1} expectedly decreases the monomer fraction in solution, and at 1 M, the monomer fraction is decreased to about 10%. Further increasing the equilibrium

constant to 146 M^{-1}, which was measured for 2H-NDI using ^{1}H-NMR, or 300 M^{-1} has a relatively small effect on the monomer fraction and at 1 M, 6% and 4% of the species exist in monomeric forms. In contrast, at a concentration of 1 mM, the large majority of the species still occur as monomers, and even when K = 300 M^{-1}, 88% of the population is unassociated. To do an electrochemical evaluation of an organic molecule only at a concentration of 1 mM thus risks overlooking self-associative effects which can be of great importance to the electrochemical behavior at higher concentrations.

4.2.2 Cyclic Voltammetry

For an ideal system, the peak current of a CV should increase linearly with the concentration according to the Randles-Sevcik equation (Equation 1). In the case of AQDS, CVs at varying concentrations, where the currents are normalized by the concentration, show decreasing currents at increasing concentrations, see Figure 4-18.

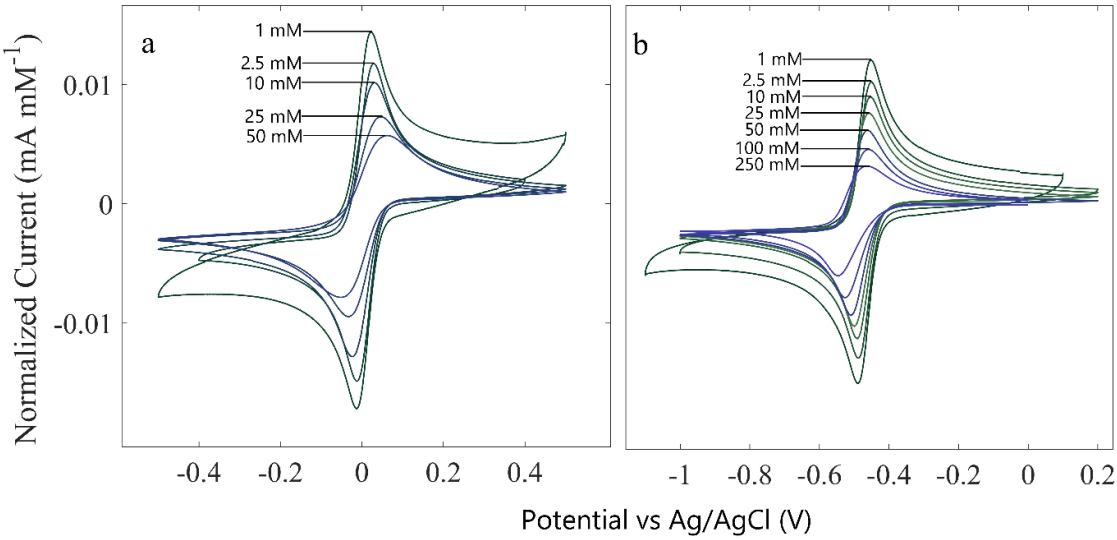

Figure 4-18: Concentration-normalized CVs of AQDS at varying concentrations in a) acid and b) pH 9.7 sodium carbonate buffer. Scan rate = 20 mV s^{-1}. (Paper I)

This indication of self-association is seen clearly in both acidic and alkaline solutions, but in acid, a peak-broadening accompanies the decrease, which complicates quantitative analysis by CV, and RDE was used instead, see Section 4.2.3. For the alkaline solution, however, the peak currents have a clear relation to the redox-accessible concentration in the solution, and when compared to monomer concentration for a self-association according to an equilibrium constant of 8 M^{-1}, excellent correlation was seen, as shown in Figure 4-19.

From these results, it was concluded that the dimer formed by AQDS is redox-inactive and has an equilibrium constant of 8 M^{-1} in the slightly alkaline 0.5 M sodium carbonate solution. If 2H-NDI, which has a much higher dimer equilibrium constant of 146 M^{-1}, behaves similarly, then a significant decrease in redox-accessible concentration would be seen on a cyclic voltammogram at increasing concentrations.

In Figure 4-20, CVs at concentrations between and 1 and 100 mM of 2H-NDI in 0.5 M phosphate buffer at pH 7 are shown. A quite steep decrease in the concentration-normalized peak currents is seen when going from the lowest concentration to 25 mM, but a further

concentration increase has a smaller impact on the redox-active concentration, and between 50 mM and 100 mM, the effect is minute.

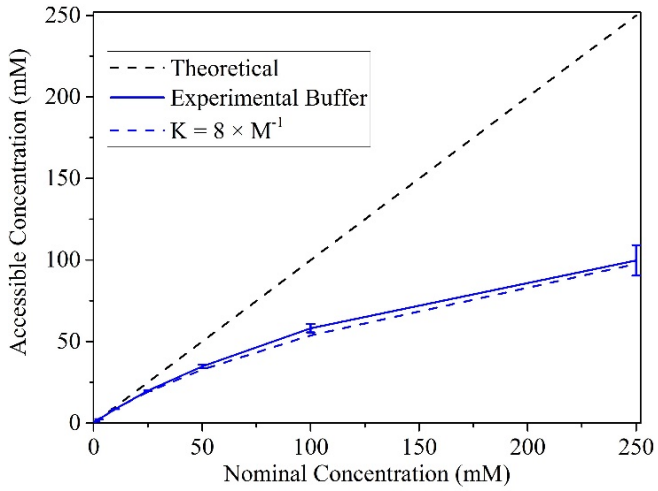

Figure 4-19: Redox-accessible concentration of AQDS in pH 9.7 sodium carbonate solution as a function of nominal concentration. The blue dashed line corresponds to the monomer concentration according to an equilibrium constant of 8 M^{-1}. (Paper I)

Furthermore, the potential for the first redox couple moves in a more positive direction at higher concentrations, while the potential for the second redox couple moves to more negative values. Similarly, this effect lessens at sufficiently high concentration, indicating that 2H-NDI seems to have a different manner of redox-hindering self-association than AQDS. However, the non-trivial shapes of the CVs for 2H-NDI hinders quantitative analysis using CV to this end, and rotating disk electrode voltammetry is used to gain further understanding of this phenomenon.

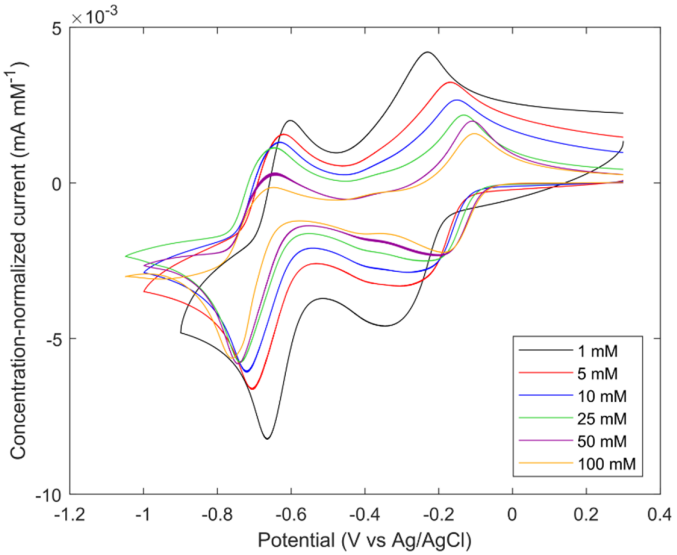

Figure 4-20: Concentration-dependent CVs of 2H-NDI in 0.5 M pH 7 sodium phosphate buffer. (Paper II)

4.2.3 Rotating Disk Electrode Voltammetry

To fortify the conclusion that AQDS forms redox-inactive dimers, RDE voltammetry was used. The limiting currents acquired in a RDE potential sweep correspond to the redox-accessible concentration and diffusion coefficient of the molecule through the Levich equation (Equation 2).

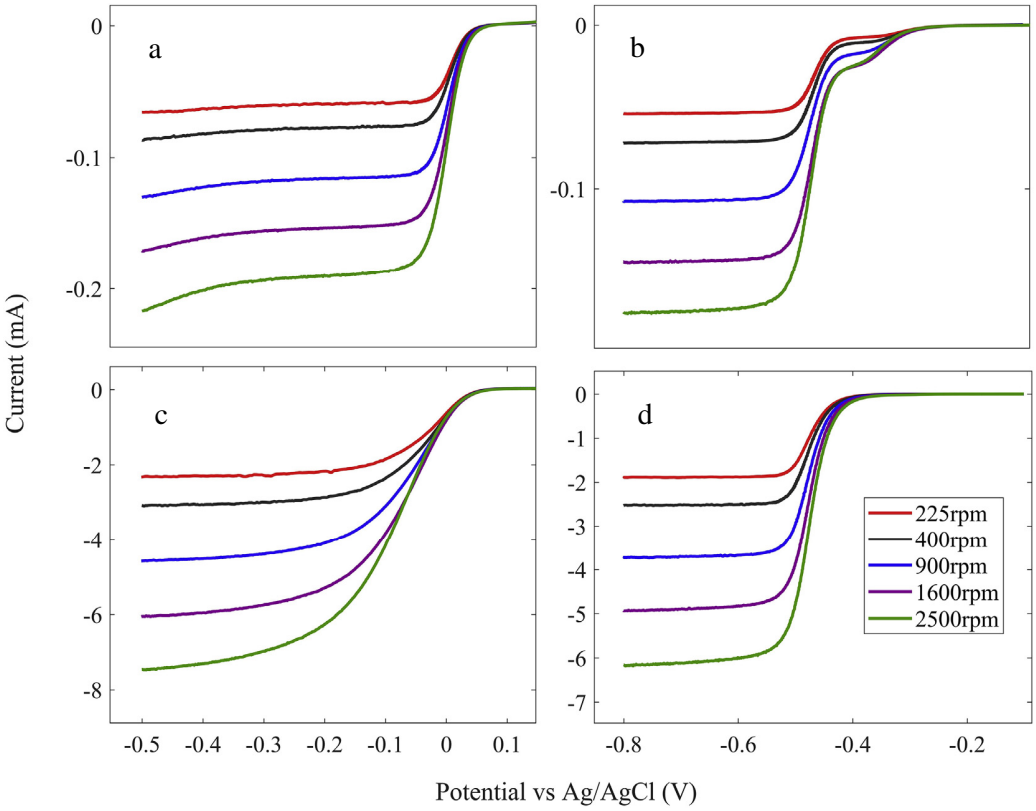

Figure 4-21: RDE voltammetry for 1 mM AQDS in a) 1 M sulfuric acid b) 0.5 M pH 9.7 sodium carbonate buffer. c) and d) show the corresponding voltammograms at 50 mM. (Paper I)

Due to the low equilibrium constant for the AQDS dimerization, it was assumed that at a concentration of 1 mM, a negligible amount of dimer is present. Therefore, the diffusion coefficient of $3.8 \cdot 10^{-6}$ cm^2 s^{-1}, which was measured using RDE voltammetry at 1 mM, was assumed to accurately represent that of the monomer. Knowing the diffusion coefficient of the monomer enabled determination of the redox-accessible concentration at higher concentrations, and RDE experiments were carried out at concentrations of 2.5, 10, 25 mM and 50 mM in both acidic and neutral solutions. The redox-accessible concentrations were found to correspond well to the calculated monomer concentrations, see Figure 4-22, and the conclusion that AQDS forms redox-inactive dimers in solution was maintained.

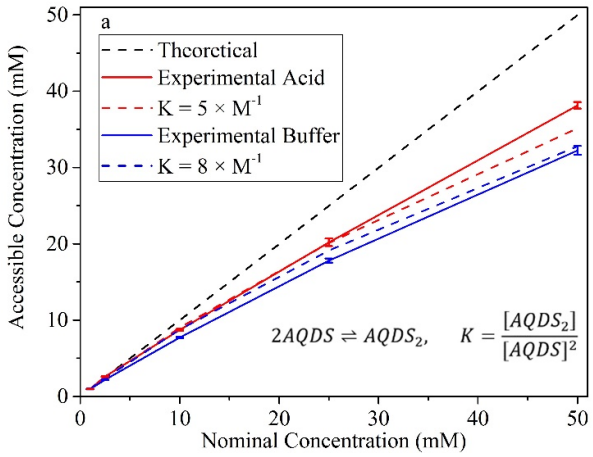

Figure 4-22: Redox-accessible concentrations and calculated monomer concentrations of AQDS in acid and alkaline buffered solution. (Paper I)

However, it needs to be noted that the dimer equilibrium established for a molecule in its fully oxidized state is disturbed upon bulk reduction and is gradually driven in the direction of dimer dissociation as monomeric AQDS is consumed. Furthermore, AQDS in its reduced state forms a dimer together with the oxidized species into what is called a quinhydrone, which complicates the self-association dynamics further.[107] Therefore, the impact of dimer formation on the redox-accessible concentration in a battery application needs further investigation.

In order to quantify how the electrochemistry of 2H-NDI is affected by self-association, RDE voltammograms for 2H-NDI were recorded at concentrations of 1, 25 and 50 mM, see Figure 4-23 for the lowest and highest concentration.

Two plateaus are seen on the voltammograms corresponding to the first and the second redox couples. At 1 mM, the Levich slope for the first electron is steeper than for the second one, and the reverse is seen at 50 mM. At 25 mM, the slopes are about equal, which is shown in the Supplementary Information of Paper II. The slopes correspond to $0.62nFA_{\mathrm{RDE}}CD^{\frac{2}{3}}\nu^{-\frac{1}{6}}$, which for AQDS, could be used to give the diffusion coefficient at 1 mM, since the redox-accessible concentration, C, could be approximated to 1 mM at a nominal concentration of 1 mM. However, as 2H-NDI significantly dimerizes already at a concentration as low as 1 mM, another analysis method was required in order to acquire the diffusion coefficient for the monomer, and diffusion NMR was chosen for this task.

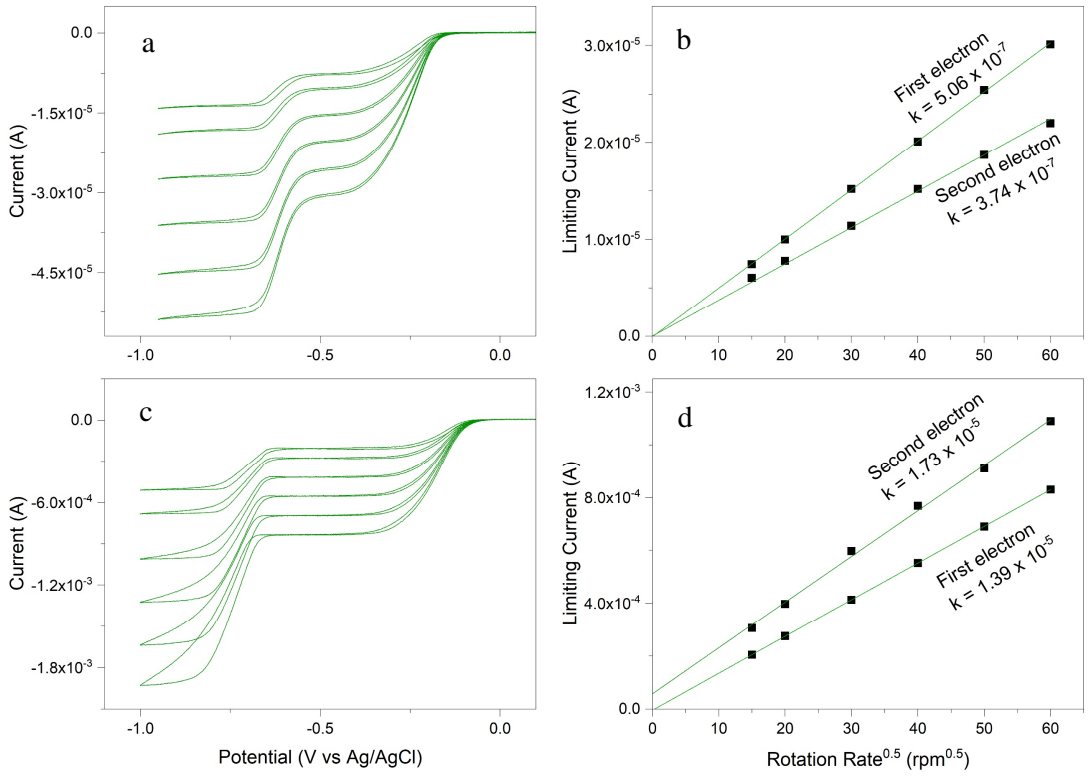

Figure 4-23: RDE voltammograms for a) 1 mM and c) 50 mM 2H-NDI in 0.5 M pH 7 sodium phosphate solution with Levich plots for the respective concentrations in b) and d). (Paper II)

4.2.4 Diffusion NMR

Self-diffusion coefficients for 2H-NDI in 0.5 M pH 7 sodium phosphate buffer in D_2O were recorded at concentrations between 1 mM and 400 mM. At the higher concentrations, the viscosity increased, which is linearly proportional to the diffusion coefficient in the absence of obstruction effects, and was therefore measured using Ubbelohde capillaries, to yield viscosity-normalized diffusion coefficients, which are presented in Figure 4-24.

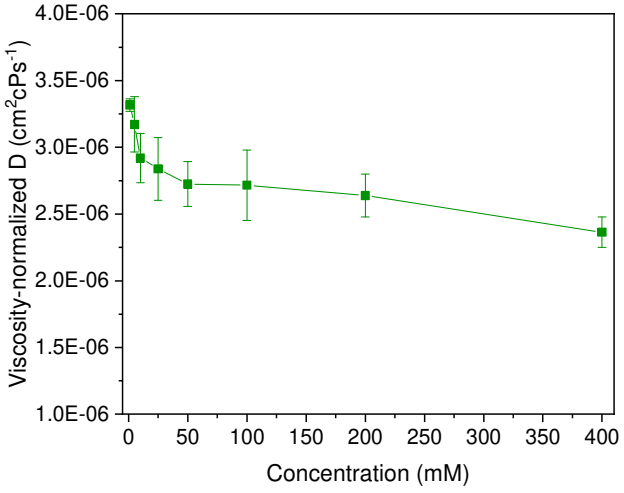

Figure 4-24: Viscosity-normalized diffusion coefficients of 2H-NDI. (Paper II)

The set of diffusion coefficients could then be used to obtain diffusion coefficients for the monomer and dimer separately according to

$$D_{\text{measured}}=\text{x}D_{monomer}+(1\text{-x})D_{\text{dimer}}, \quad 14$$

where x is the fraction of monomer present in solution.

Since the diffusion coefficients were measured in deuterated water which is approximately 20% more viscous than normal water, viscosities were measured for the corresponding solutions in normal water and corrected using the Stokes-Einstein equation:

$$D=\frac{k_{\text{B}}T}{6\pi\eta r}, \quad 15$$

and lastly used to acquire the redox-accessible concentrations using a modified version of Equation 2:

$$i_{\text{l}}\omega^{-\frac{1}{2}}=0.62FA_{\text{RDE}}(n_{\text{m}}C_{\text{m}}D_{\text{m}}^{\frac{2}{3}}+n_{\text{d}}C_{\text{d}}D_{\text{d}}^{\frac{2}{3}})\nu^{-\frac{1}{6}}, \quad 16$$

which handles the current contributions from the monomer and dimer separately.

Inserting different numbers of electrons for the dimer, n_{d}, into Equation 16 showed that during the first reduction, the dimer is only reduced with one electron instead of the expected two, which would have corresponded to double the amount of the monomer. However, since the dimer equilibrium is disturbed once the radical anion, 2H-NDI$^{-\bullet}$ has been formed, only the dynamics of the first electron could be handled in this manner.

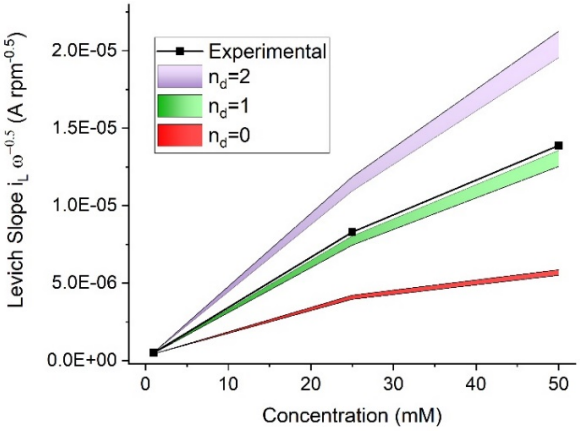

Figure 4-25: Levich slopes for the first reduction of 2H-NDI to 2H-NDI$^{-\bullet}$ in 0.5 M pH 7 sodium phosphate solution. Experimental values are shown by the black markers, and the colored intervals show calculated values acquired from Equation 16 using different number of electrons for the dimer. (Paper II)

To summarize Section 4.2, AQDS dimerizes to a smaller degree than 2H-NDI, but has a completely redox-inactive dimer, whereas 2H-NDI has a much stronger self-association than AQDS, but its dimer retains limited redox-activity.

4.3 Cyclic Voltammetry and Bulk Electrolysis at High Concentration

The AQDS dimerization is known to hinder its redox activity in bulk electrolysis conditions so that only a fraction of the theoretical capacity can be accessed.[52, 53] For example, in Figure

4-26, 50 mM AQDS in 1 M sulfuric acid was reduced and oxidized galvanostatically, and only 60% of the theoretical capacity was accessed.

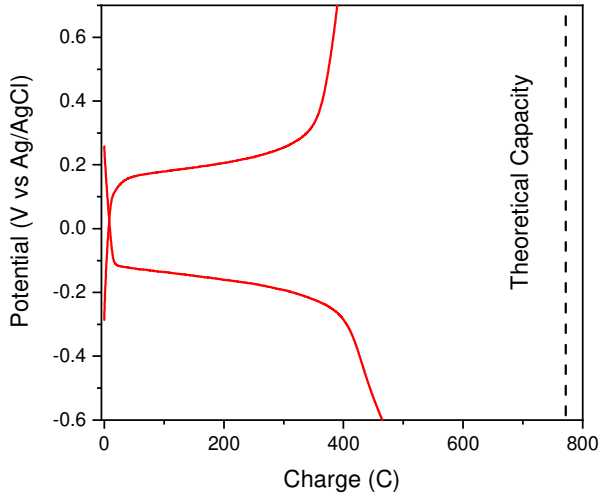

Figure 4-26: Bulk electrolysis of 50 mM AQDS in 1 M sulfuric acid. Current: 31.1 mA.

Conversely, in the galvanostatic cycling experiments shown in Figure 4-27 and Figure 4-28, 2H-NDI was cycled with high capacity utilizations.

At 25 mM, the majority of the 2H-NDI molecules are present as dimers, but close to the full amount of the theoretical capacity was reached regardless, indicating that the dimers decreasing the redox-activity dissociate quickly enough not to significantly affect bulk electrolysis behavior.

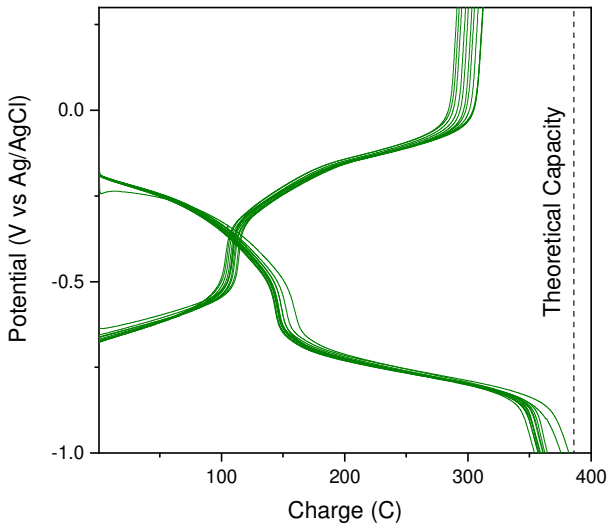

Figure 4-27: Bulk electrolytic cycling of 25 mM 2H-NDI in pH 7 sodium phosphate buffer. Current: 15 mA. (Paper II)

A slightly higher amount of charge on the reduction than on the oxidation was passed. While 2H-NDI is reduced on the working electrode, water is oxidized on the counter electrode, which is separated from the bulk solution by a glass frit, and oxygen is generated. The generated oxygen can in turn diffuse to the bulk solution, oxidize the reduced 2H-NDI back to the starting

material and incur a decrease in coulombic efficiency. A second explanation is that some water was reduced, and the parasitic HER occurred. Interestingly, the charge of the first potential plateau during reduction, which corresponding to the reduction of 2H-NDI to 2H-NDI$^{-\bullet}$, is lower than the charge for 2H-NDI$^{-\bullet}$ to 2H-NDI^{2-}. The opposite behavior is then seen on the oxidation, where the plateau for 2H-NDI^{2-} to 2H-NDI$^{-\bullet}$ reaches a lower charge than that for 2H-NDI$^{-\bullet}$ to 2H-NDI.

Following this, a bulk electrolysis experiment of 15 mM 2H-NDI was carried out in 1 M H_2SO_4, see Figure 4-28. A higher charge than calculated for 15 mM 2H-NDI in 80 ml of solution was passed, likely due to the HER. But more interestingly, the plateau of the following oxidative sweep was at a potential significantly more positive than expected. The computational results in Section 4.1.2 were useful in explaining this behavior. After accommodating two electrons, the pK_a values of 2H-NDI^{2-} were calculated to be 2.90 and 0.45 to form 2H-NDIH$^-$ and 2H-NDIH$_2$ respectively. At pH 0, most of the reduced 2H-NDI species would thus be doubly protonated, and since the calculated pK_a values tended to be slightly underestimated (more information about this is found in Paper III), this equilibrium is likely shifted even further in the direction of protonation. The computationally acquired reduction potential of 2H-NDIH$_2$ was 0.48 V vs NHE, which would correspond reasonably well to an oxidation plateau at about 0.75 V vs RHE, when taking the overpotential into consideration. Summarily, at pH 0, the reductive pathway of 2H-NDI seems to be $E_1E_2C_3C_6$, but the oxidative pathway $E_6C_5C_2E_1$.

2Br-NDI could not be dissolved in any other electrolyte than 1 M sulfuric acid, and therefore, 15 mM 2Br-NDI was cycled in a bulk electrolysis cell at pH 0 in 1 M sulfuric acid, as shown in Figure 4-28.

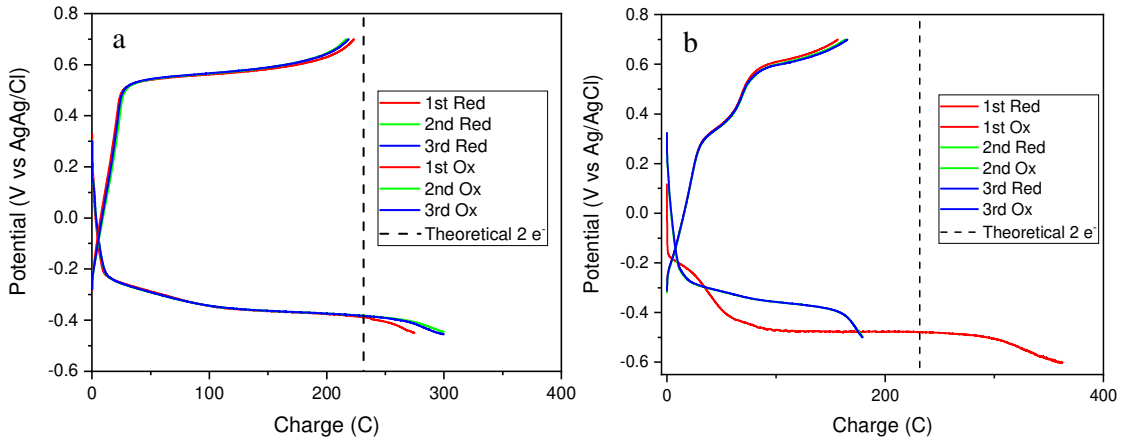

Figure 4-28: Bulk electrolysis cycling of a) 2H-NDI and b) 2Br-NDI in 1 M sulfuric acid. Current: 25 mA. The green lines corresponding to the second cycle are hidden behind those of the third cycle.

First a small reduction plateau is seen, followed by a much longer second plateau at a more negative potential. The second plateau progresses significantly beyond the charge expected for two electrons before turning down towards more negative potentials and presumably beginning a third plateau corresponding to the HER. The following oxidation shows the same behavior as 2H-NDI and occurs at a much more positive potential than does the reduction. After this point, the system cycles reversibly with as close to theoretical capacities as is expected from a bulk electrolysis cell. It is thus likely that 2Br-NDI is electrolytically converted into 2H-NDI

upon reduction. This would also explain the smaller oxidative peak currents on the CV in Figure 4-5a.

A part of the electrolyte was removed from the cell, neutralized and shaken together with dichloromethane. The 2Br-NDI species, or any electrolysis products with a propyl-dimethylamino sidechain were thus extracted into the organic solvent. The organic phase was dried, and the remains were dissolved in deuterated chloroform and examined by ^{1}H-NMR spectroscopy. The spectrum was compared to both pure 2H-NDI and 2Br-NDI which is shown in Figure 4-29. From this experiment, it was concluded that 2Br-NDI is converted to 2H-NDI upon reduction and unsuitable for redox flow battery application.

It should be noted that after failing to dissolve 2Br-NDI in 1 M hydrochloric acid, the solution was neutralized and extracted into chloroform, and the 2Br-NDI was quantitatively recovered using this treatment. Consequently, if any 2Br-NDI had remained in the bulk electrolysis cell after cycling, it would have been visible in the middle spectrum of Figure 4-29.

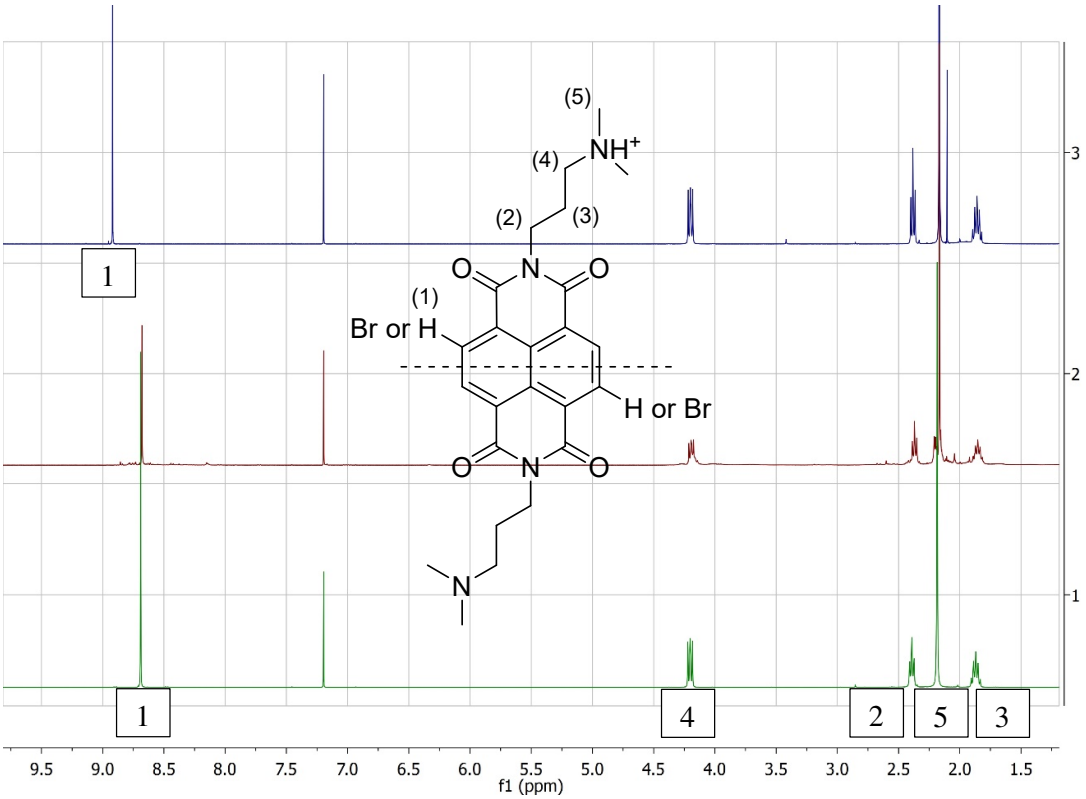

Figure 4-29: Assigned ^{1}H-NMR spectra of 2H-NDI (bottom), extracted 2Br-NDI after bulk electrolysis (middle) and 2Br-NDI (top) in chloroform.

In the case of 2DMA-NDI, it was hypothesized that the dimethylamine substituents on the naphthalene core would sterically hinder self-association, and more ideal concentration-dependent electrochemistry would be observed. However, in the concentration-normalized CVs in Figure 4-30, a decrease is concentration-normalized peak currents is clearly seen, although for 1 mM, one must extrapolate the value from the baseline.

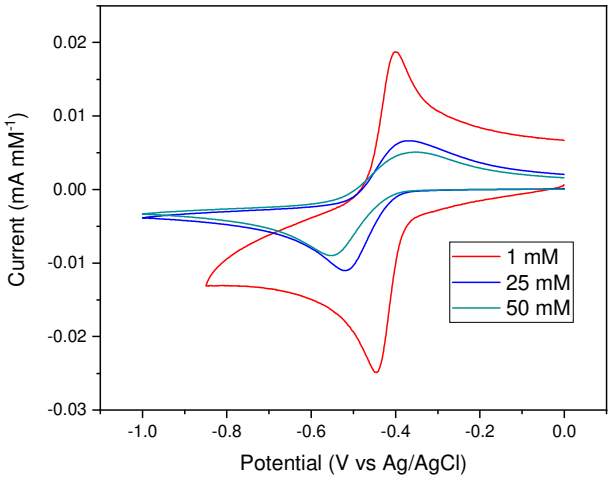

Figure 4-30: Concentration-normalized CVs for 1, 25 and 50 mM of 2DMA-NDI in 0.5 M sodium phosphate neutral buffer. Sweep rate: 100 mV s^{-1}.

Figure 4-31 shows that 2DMA-NDI has a different sweep rate-dependence at 1 and 50 mM in neutral 0.5 M sodium phosphate solution. At 1 mM, the reductive peak current increases somewhat, at increasing sweep rate, and also moves in the negative direction. For the oxidative peak, the normalized current increases marginally, but is not significantly shifted in potential. At increasing the concentration to 50 mM, a significant peak-broadening for both the reductive and oxidative peaks can be seen along with an increase in peak separation.

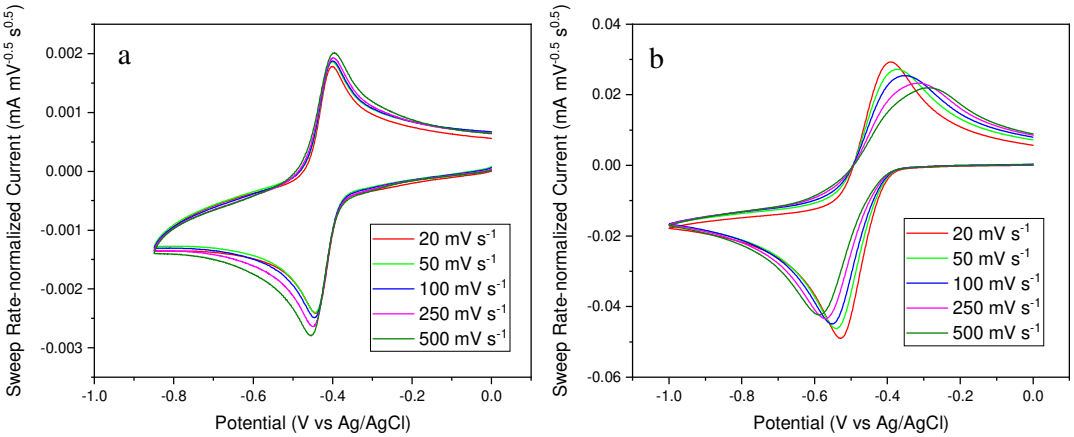

Figure 4-31: Sweep rate-normalized CVs for a) 1 mM 2DMA-NDI (same as Figure 4-8b) and b) 50 mM 2DMA-NDI in 0.5 M pH 7 sodium phosphate buffer. (Paper III and Paper IV)

To better understand the reason behind the sweep rate-dependence of the CV in Figure 4-31b, two additional CVs of 50 mM 2DMA-NDI were recorded, one in pH 7 0.5 M potassium phosphate (KPh) and 1 M potassium chloride (KCl), and one in pH 7 0.5 M ammonium phosphate (AmPh) and 1 M ammonium chloride (AmCl), see Figure 4-32. Interestingly, all three CVs at 50 mM behave quite differently depending on the electrolyte. The combined results shown in Figure 4-30, Figure 4-31 and Figure 4-32 give a strong indication that self-associative effects play a role in the electrochemistry of 2DMA-NDI.

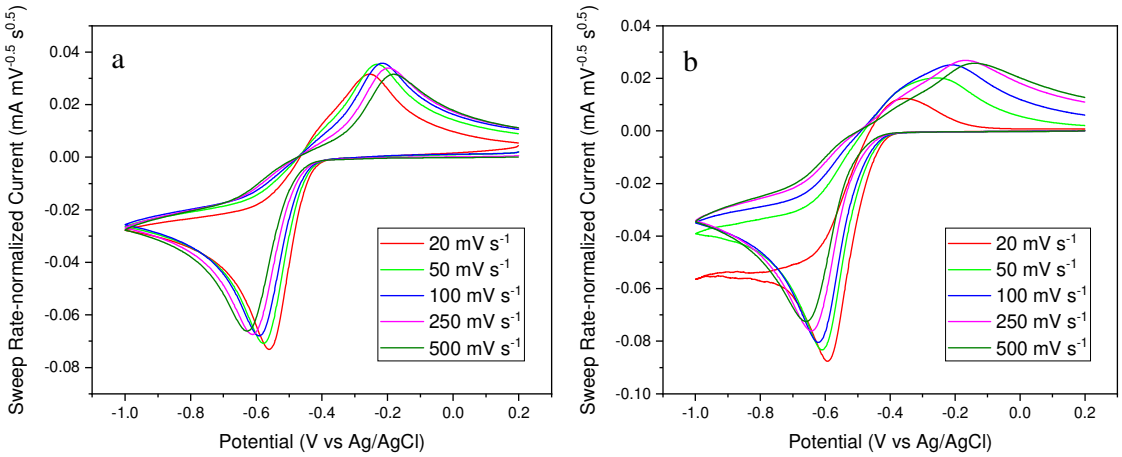

Figure 4-32: Sweep rate-normalized CVs of 50 mM 2DMA-NDI in pH 7 a) 0.5 M KPh and 1 M KCl and b) 0.5 M AmPh and 1 M AmCl.

Galvanostatic cycling of 15 mM 2DMA-NDI in 80 ml pH 7 sodium phosphate solution in a bulk electrolysis cell is shown in Figure 4-33. About 80% of the theoretical capacity is accessed on the reductive hold, and about 70% on the oxidation. These inefficiencies, however, are not as telling in a bulk electrolysis cell as in an actual redox flow battery, due to the possibility of oxidation, either by oxygen generated on the counter electrode, or by atmospheric oxygen leaking into the solution. Therefore, a judgement on the coulombic efficiency of 2DMA-NDI is reserved for the following section. Relatively small differences are seen between the cycles, signifying good chemical stability of the molecule. Thus, 2DMA-NDI is shown to be an interesting candidate for a redox flow battery test, despite its idiosyncratic behavior on the CV timescale.

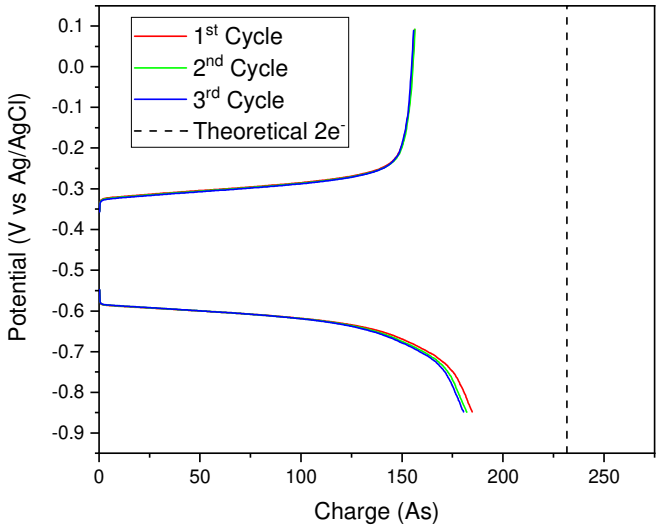

Figure 4-33: Bulk electrolytic cycling of 15 mM 2DMA-NDI in 80 ml 0.5 M sodium phosphate solution at pH 7. Current: 50 mA.

4.4 Redox Flow Battery Cycling

Five redox flow battery chemistries were tested and are presented in Table 4-4.

Table 4-4: Studied NDI-based redox flow battery chemistries. (Paper IV)

#	Conc.	Negolyte	Electrolyte	Voltage[a]	Ohmic resistance	Cycling time
1	50 mM	2H-NDI / Fc[b]	1 M KCl + 0.5 M KPh[b]	0.65 V	0.63 Ohm	192 hours
2	50 mM	2H-NDI / Fc	1 M AmCl[b] + 0.5 M AmPh	0.67 V	1.07 Ohm	156 hours
3	500 mM	2H-NDI / Fc	1 M AmCl + 0.5 M AmPh	0.65 V	0.66 Ohm	212 hours
4	50 mM	2DMA-NDI / Fc	1 M KCl + 0.5 M KPh	0.62 V	0.57 Ohm	88 hours
5	50 mM	2DMA-NDI / Fc	1 M AmCl + 0.5 M AmPh	0.65 V	0.67 Ohm	173 hours

[a] *Calculated from the average charge and discharge voltages.*

[b] *Fc=BTMAP-Fc, Am = Ammonium, Ph = Phosphate.*

Each battery was assembled, charged and discharged three times at varying current densities, and then cycled at a given current density for a longer period of time. To balance the capacities of each side, the negative reservoir contained 10 ml of NDI electrolyte, while the positive reservoir contained 20 ml of the ferrocene. Charging, in the present context, corresponds to the reduction of NDI, the oxidation of BTMAP-Fc, and an increasing cell potential, and vice versa for discharging.

4.4.1 Battery Performance of 2H-NDI

Two pH-neutral redox flow batteries using equimolar solutions of 50 mM 2H-NDI and BTMAP-Fc were assembled. One had a supporting electrolyte consisting of 1 M potassium chloride (KCl) and 0.5 M potassium phosphate (KPh), and the other had one of 1 M ammonium chloride (AmCl) and 0.5 M ammonium phosphate (AmPh).

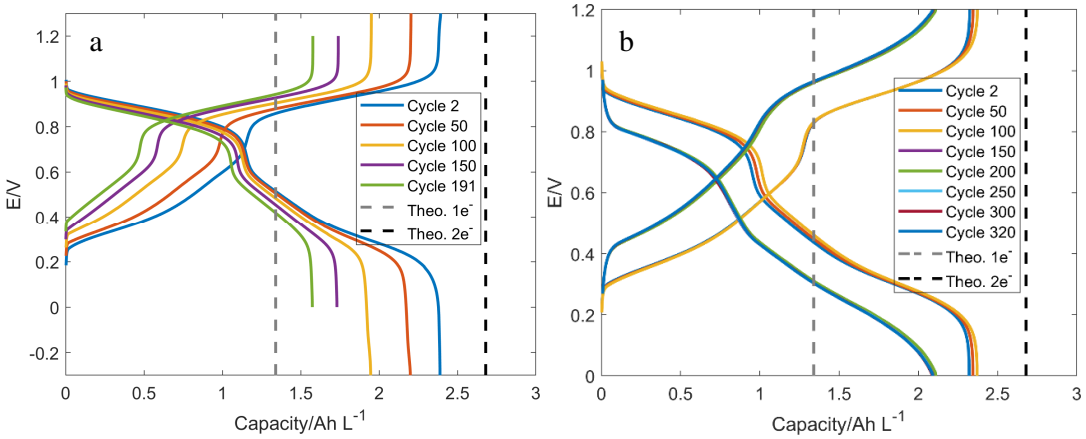

Figure 4-34: Charge and discharge curves of 50 mM 2H-NDI/BTMAP-Fc in a) 1 M KCl and 0.5 M KPh and b) 1 M AmCl and 0.5 M AmPh. (Paper IV)

Charge and discharge curves for the two batteries are shown Figure 4-34. For the potassium-based battery, the capacity of the first charging plateau is significantly smaller than that of the second plateau, similar to what was seen on the bulk electrolysis curves in Figure 4-27. By taking the steepest point of the curve (around 0.7 V) as the transition between the first and the second plateau, the trend could be quantified, see Figure 4-35b, where the capacities are normalized against the theoretical value for one electron. During cycling, the capacity corresponding to the first redox couple, in other words, the reaction 2H-NDI + e^- ⇌ 2H-NDI$^{\bullet}$,

decreases quite rapidly relative to the capacity corresponding to the second redox couple, or $2H\text{-}NDI^{-\bullet} + e^- \rightleftharpoons 2H\text{-}NDI^{2-}$. Furthermore, the difference in capacity between each plateau when charging and discharging decreases slightly, perhaps accompanied by a subtle increase in energy efficiency, see Figure 4-35a. The cause of this selective capacity loss is thought to be binding of potassium ions to $2H\text{-}NDI^{2-}$, as has been previously reported for a similar phenomenon.[63] After 143 cycles at 10 mA cm^{-2}, the current density was decreased to 5 mA cm^{-2}, but no amelioration of the capacity loss in Figure 4-35a was seen.

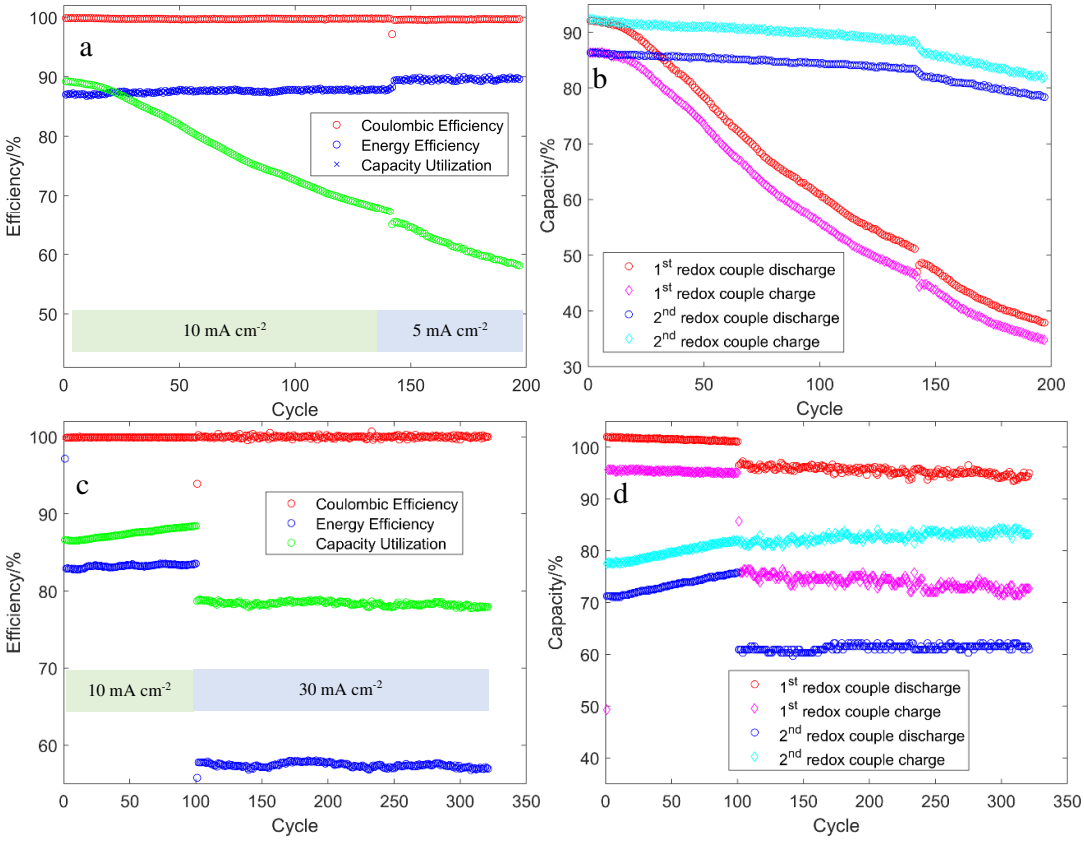

Figure 4-35: Redox flow battery performance of 50 mM 2H-NDI/BTMAP-Fc in 1 M KCl and 0.5 M KPh (upper) and 1 M AmCl and 0.5 M AmPh (lower). a) and c) Efficiencies. b) and d) capacity utilizations of the voltage plateaus for the first and second electrons during charge and discharge. (Paper IV)

Interestingly, the opposite trend is seen for the battery with the ammonium-based supporting electrolyte, perhaps due to a different binding interaction between $2H\text{-}NDI^{-2}$ and the ammonium ions compared to potassium. Furthermore, the loss of capacity that was seen for the potassium-based battery in Figure 4-35a was replaced by a small increase in capacity over 100 cycles at 10 mA cm^{-2}, see Figure 4-35c. The increase in capacity is possibly due to the electrochemical activation of the unpretreated carbon electrodes.[108] After 100 cycles, the current density increased to 30 mA cm^{-2} for 220 cycles, and a very high level of stability is observed. Interestingly, the capacity utilization corresponding to all redox couple was decreased upon increasing the current density with the exception of the second redox couple during charging, which accessed the same capacity. The second redox couple during charging

corresponds to the forward reaction of $2H\text{-}NDI^{-\bullet} + e^- \rightleftharpoons 2H\text{-}NDI^{2-}$, which thus seemed to be favored at higher current densities.

To see if the 2H-NDI performs well even at higher concentrations, a 500 mM 2H-NDI/BTMAP-Fc battery with 1 M AmCl and 0.5 M AmPh was assembled. The selective capacity loss seen in the first battery was again observed, and 15% capacity was lost over 58 cycles. More information on this can be found in Paper IV.

4.4.2 Battery Performance of 2DMA-NDI

Batteries with 50 mM 2DMA-NDI/BTMAP-Fc using the same background electrolytes as in Section 4.4.1 were assembled, to study the applicability of 2DMA-NDI for use in redox flow batteries.

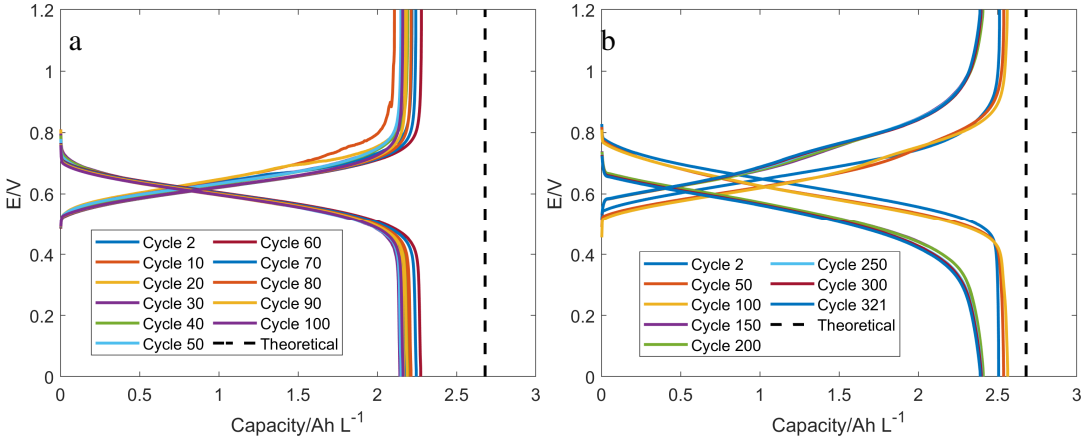

Figure 4-36: Charge and discharge curves of 50 mM 2DMA-NDI/BTMAP-Fc in a) 1 M KCl and 0.5 M KPh and b) 1 M AmCl and 0.5 M AmPh. (Paper IV)

Figure 4-36 shows charge and discharge curves for the two batteries. As 2DMA-NDI only has one two-electron redox couple, only one plateau is seen on the curves. For the potassium-based battery, a flow disturbance caused erratic data, but once the disturbance was amended, the results stabilized. For the last 40 cycles, the capacity utilization decreases by 5%, but a high energy efficiency of 92% was seen, see Figure 4-37a.

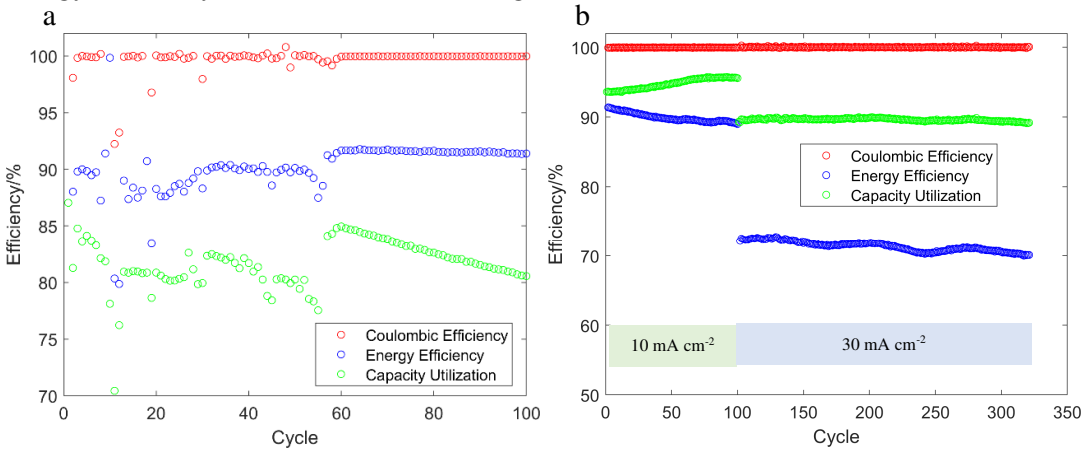

Figure 4-37: Redox flow battery performance of 50 mM 2DMA-NDI/BTMAP-Fc in a) 1 M KCl and 0.5 M KPh and b) 1 M AmCl and 0.5 M AmPh. (Paper IV)

Similar to 2H-NDI, the ammonium-based electrolyte brought a large increase in cycling stability for the 2DMA-NDI/BTMAP-Fc battery, compared to the potassium-based one. Over the first 100 cycles at a current density of 10 mA cm^{-2}, the capacity increased, and following this, over 220 cycles at 30 mA cm^{-2}, no capacity loss was detected, see Figure 4-37b.

5 Conclusions and Outlook

While aqueous organic redox flow batteries hold great promise to provide environmentally friendly energy storage, long-term cycling stability and low energy densities remain challenges to overcome. Batteries using AQDS suffer from low capacity utilizations due to self-association, a phenomenon that is easy to overlook when doing electrochemical studies only at low concentrations. 2H-NDI showed a larger affinity to self-associate than did AQDS, but its redox activity was less affected by the self-association. By combining diffusion NMR and rotating disk electrode voltammetry, it was seen that 2H-NDI forms a dimer that has a limited redox-activity on the CV timescale. Unlike AQDS, however, most of its theoretical capacity could be accessed in bulk electrolysis.

Nine core-substituted NDI species were examined computationally using DFT, and three of them we examined experimentally using cyclic voltammetry. From this, mechanistic information could be gained for the different species, bringing understanding of the fundamental electrochemistry of 2X-NDI. Five of the nine species were identified as of special interest, two of which were studied in redox flow batteries with varying background electrolytes.

The two batteries using 50 mM 2H-NDI or 2DMA-NDI coupled with BTMAP-Fc performed excellently in 1 M AmCl and 0.5 M AmPh, demonstrating astonishing cycling stability. Conversely, the same molecules in 1 M KCl and 0.5 KPh suffered from a significant capacity loss while cycling, which in the case of 2H-NDI was attributed to the binding of potassium ions to the doubly reduced state, $2H\text{-}NDI^{2-}$.

Information regarding stability on the scale of months or years is still lacking and would be necessary for the technology to progress. Moreover, further work is needed on establishing a high level of cycling stability at high concentrations of active material.

6 Acknowledgements

Firstly, a heartfelt thanks to anyone who reads this doctoral thesis, perhaps all the way from the start to the acknowledgements section. Research is given meaning through the dissemination of the results and of the lessons learned. So, after spending four-and-a-quarter years on this book and on this research, I am sincerely grateful to any reader who finds anything useful in these pages, and thus gives my work some meaning beyond self-gratification.

My family has always been there as a buttress, even when I have been overcome by the frustration of banging my head against the wall that research sometimes is. My mother and father are the only two people outside of academia that I have relied on for help with my research. Thank you for all the love, patience and food you have given me.

I quickly learned that research is very demanding. One must be painstakingly careful and forge one's discipline into the hardest steel in order to succeed in the fierce competition. Although I am not sure this is an apt description of myself, it fits Professor Elisabet Ahlberg like a hand in glove. She has taught me the importance of a solid foundation before building too high, and how surprisingly exciting it can be to look in every nook and cranny of my data for clues on how the pieces of the puzzle fit together. For this, I will always be grateful.

Professor Lars Nordstierna has been invaluable by bringing a different perspective to my research. Problems I had been struggling with for days or weeks, he had a way of solving with just a word. Thank you, Lars, for your supervision, help, and warmth.

During my research, I have had the pleasure of interacting with many inspiring professors, to whom I profess my utmost respect and appreciation. Special thanks to Professors Hanna Härelind, Per Lincoln, Martin Andersson, Fikile Brushett, Jerker Mårtensson, Anders Palmqvist, Zareen Abbas, Ergang Wang, Anette Larsson, Christian Müller and Kasper Moth-Poulsen.

A big thank you to all the inspiring and special people I have met at Chalmers and Gothenburg University, who, I am grateful to say, are too many to count. I will always count Sarah, Emmy, Sepideh, Alicja, Anna (take a pick), Alex, Richard, Alica, Clara, Isabelle, Christian, Julien, Peter, Johanna, Ting and Justas as close friends. The shrewd reader will notice that the order of the names roughly matches the distance between my office and theirs. Thank you, Mariza, for making the beautiful cover and being a great friend.

Finally, I am sure that nobody at the Department of Chemistry and Chemical Engineering would manage to dissertate without Lotta Pettersson, who administers candy, compliments and contracts like no one else. I am glad I don't have to answer your Friday-quiz-questions during my dissertation.

7 References

1. Wiberg, C. Aqueous Organic Redox Flow Batteries - Electrochemical studies of quinonoid compounds. Chalmers University of Technology, Gothenburg, 2019.

2. Arrhenius, S., (1896). XXXI. On the influence of carbonic acid in the air upon the temperature of the ground. *The London, Edinburgh, and Dublin Philosophical Magazine and Journal of Science* 41, 251, 237-276.

3. Etheridge, D. M.; Steele, L. P.; Langenfelds, R. L.; Francey, R. J.; Barnola, J. M.; Morgan, V. I., (1996). Natural and anthropogenic changes in atmospheric CO2over the last 1000 years from air in Antarctic ice and firn. *Journal of Geophysical Research: Atmospheres* 101, D2, 4115-4128.

4. MacFarling Meure, C.; Etheridge, D.; Trudinger, C.; Steele, P.; Langenfelds, R.; van Ommen, T.; Smith, A.; Elkins, J., (2006). Law Dome CO2, CH4and N2O ice core records extended to 2000 years BP. *Geophysical Research Letters* 33, 14.

5. Zachos, J.; Pagani, M.; Sloan, L.; Thomas, E.; Billups, K., (2001). Trends, Rhythms, and Aberrations in Global Climate 65 Ma to Present. *Science* 292, 5517, 686-693.

6. Frakes, L. A.; Francis, J. E.; Syktus, J. I., *Climate Modes of the Phanerozoic*. Cambridge University Press: Cambridge, 1992.

7. Hartfield, G.; Blunden, J.; Arndt, D. S., (2018). State of the Climate in 2017. *Bulletin of the American Meteorological Society* 99, 8, Si-S310.

8. Tans, P. K., Ralph CO2 data from Mauna Loa. https://www.esrl.noaa.gov/gmd/ccgg/trends/

9. NASA's Goddard Institute for Space Studies (GISS). https://climate.nasa.gov/vital-signs/global-temperature/

10. Boer, M. M.; Dios, V. R. d.; Bradstock, R. A., (2020). Unprecedented burn area of Australian mega forest fires. *Nature Climate Change* 10, 3, 171-172.

11. (8 January 2020). More than one billion animals killed in Australian bushfires. *The University of Sydney*.

12. O'Gorman, D., (2020). Statement from WWF-Australia on Australia's bushfire emergency.

13. Voiland, A., Heat and Fire Scorches Siberia. *The Earth Observatory* 23 June 2020, 2020.

14. Kim, J.-S.; Kug, J.-S.; Jeong, S.-J.; Park, H.; Schaepman-Strub, G., (2020). Extensive fires in southeastern Siberian permafrost linked to preceding Arctic Oscillation. *Science Advances* 6, 2, eaax3308.

15. Svensson, J.; Virkkula, A.; Meinander, O.; Kivekäs, N.; H.-R, H.; O, J.; J.I, P.; Gritsevich, M.; Heikkilä, A.; Kontu, A.; Neitola, K.; D, B.; Waldhauserova, P.; K, A.; Vehkamäki, M.; Hienola, A.; de

Leeuw, G.; Lihavainen, H., (2016). Soot-doped natural snow and its albedo - Results from field experiments. *Boreal Environment Research* 28, 481–503.

16. Hartmann, D. L., Chapter 10 - Climate Sensitivity and Feedback Mechanisms. In *Global Physical Climatology (Second Edition)*, Hartmann, D. L., Ed. Elsevier: Boston, 2016; pp 293-323.

17. *Inventory of U.S. Greenhouse Gas Emissions and Sinks: 1990-2018*; EPA 430-R-20-002; United States Environmental Protection Agency: April 13, 2020, 2020.

18. *Renewables 2020 Global Status Report*; REN21: 2020.

19. (2018). Renewable Energy Policy Network for the 21st Century (REN21).

20. Izumi, M. G. K. *Trends 2018 in Photovoltaic Applications*; T1-34:2018; IEA International Energy Agency: 2018.

21. *Annual Market Update 2017 - Global Wind Report*; Global Wind Energy Council: 2017.

22. Solomon, A. A.; Bogdanov, D.; Breyer, C., (2019). Curtailment-storage-penetration nexus in the energy transition. *Applied Energy* 235, 1351-1368.

23. Narayanan, A.; Mets, K.; Strobbe, M.; Develder, C., (2019). Feasibility of 100% renewable energy-based electricity production for cities with storage and flexibility. *Renewable Energy* 134, 698-709.

24. (IRENA), I. R. E. A. *IRENA (2020), Global Renewables Outlook: Energy transformation 2050*; International Renewable Energy Agency (IRENA): 2020.

25. Liu, W.; Lu, W.; Zhang, H.; Li, X., (2019). Aqueous Flow Batteries: Research and Development. *Chemistry – A European Journal* 25, 1649-64.

26. Weber, A. Z.; Mench, M. M.; Meyers, J. P.; Ross, P. N.; Gostick, J. T.; Liu, Q., (2011). Redox flow batteries: a review. *J. Appl. Electrochem.* 41, 10, 1137-1164.

27. Rychcik, M.; Skyllas-Kazacos, M., (1988). Characteristics of a new all-vanadium redox flow battery. *J. Power Sources* 22, 1, 59-67.

28. Huskinson, B.; Marshak, M. P.; Suh, C.; Er, S.; Gerhardt, M. R.; Galvin, C. J.; Chen, X.; Aspuru-Guzik, A.; Gordon, R. G.; Aziz, M. J., (2014). A metal-free organic-inorganic aqueous flow battery. *Nature* 505, 7482, 195-8.

29. Minke, C.; Kunz, U.; Turek, T., (2017). Carbon felt and carbon fiber - A techno-economic assessment of felt electrodes for redox flow battery applications. *J. Power Sources* 342, 116-124.

30. Wang, W.; Luo, Q.; Li, B.; Wei, X.; Li, L.; Yang, Z., (2013). Recent Progress in Redox Flow Battery Research and Development. *Adv. Funct. Mater.* 23, 8, 970-986.

31. Maurya, S.; Shin, S.-H.; Kim, Y.; Moon, S.-H., (2015). A review on recent developments of anion exchange membranes for fuel cells and redox flow batteries. *RSC Advances* 5, 47, 37206-37230.

32. Yuan, Z.; Zhang, H.; Li, X., (2018). Ion conducting membranes for aqueous flow battery systems. *Chem Commun (Camb)* 54, 55, 7570-7588.

33. Ye, R.; Henkensmeier, D.; Yoon, S. J.; Huang, Z.; Kim, D. K.; Chang, Z.; Kim, S.; Chen, R., (2017). Redox Flow Batteries for Energy Storage: A Technology Review. *Journal of Electrochemical Energy Conversion and Storage* 15, 1, 010801.

34. Xu, J.; Thomas, H. R.; Francis, R. W.; Lum, K. R.; Wang, J.; Liang, B., (2008). A review of processes and technologies for the recycling of lithium-ion secondary batteries. *J. Power Sources* 177, 2, 512-527.

35. Ordoñez, J.; Gago, E. J.; Girard, A., (2016). Processes and technologies for the recycling and recovery of spent lithium-ion batteries. *Renewable and Sustainable Energy Reviews* 60, 195-205.

36. Blomgren, G. E., (2017). The development and future of lithium ion batteries. *J. Electrochem. Soc.* 164, 1, A5019-A5025.

37. Doughty, H. D. *Vehicle Battery Safety Roadmap Guidance*; National Renewable Energy Laboratory: 2012.

38. Mao, B.; Huang, P.; Chen, H.; Wang, Q.; Sun, J., (2020). Self-heating reaction and thermal runaway criticality of the lithium ion battery. *Int. J. Heat Mass Transfer* 149.

39. Wu, M. C.; Zhao, T. S.; Jiang, H. R.; Zeng, Y. K.; Ren, Y. X., (2017). High-performance zinc bromine flow battery via improved design of electrolyte and electrode. *J. Power Sources* 355, 62-68.

40. Zheng, M.; Sun, J.; Meinrenken, C. J.; Wang, T., (2018). Pathways Toward Enhanced Techno-Economic Performance of Flow Battery Systems in Energy System Applications. *Journal of Electrochemical Energy Conversion and Storage* 16, 2, 021001-021001-11.

41. Zhang, M.; Moore, M.; Watson, J. S.; Zawodzinski, T. A.; Counce, R. M., (2012). Capital Cost Sensitivity Analysis of an All-Vanadium Redox-Flow Battery. *J. Electrochem. Soc.* 159, 8, A1183-A1188.

42. Leung, P.; Shah, A. A.; Sanz, L.; Flox, C.; Morante, J. R.; Xu, Q.; Mohamed, M. R.; Ponce de León, C.; Walsh, F. C., (2017). Recent developments in organic redox flow batteries: A critical review. *J. Power Sources* 360, 243-283.

43. Pan, F.; Wang, Q., (2015). Redox Species of Redox Flow Batteries: A Review. *Molecules* 20, 11, 20499-517.

44. Darling, R. M.; Gallagher, K. G.; Kowalski, J. A.; Ha, S.; Brushett, F. R., (2014). Pathways to low-cost electrochemical energy storage: a comparison of aqueous and nonaqueous flow batteries. *Energy Environ. Sci.* 7, 11, 3459-3477.

45. Dmello, R.; Milshtein, J. D.; Brushett, F. R.; Smith, K. C., (2016). Cost-driven materials selection criteria for redox flow battery electrolytes. *J. Power Sources* 330, 261-272.

46. Wei, X.; Pan, W.; Duan, W.; Hollas, A.; Yang, Z.; Li, B.; Nie, Z.; Liu, J.; Reed, D.; Wang, W.; Sprenkle, V., (2017). Materials and Systems for Organic Redox Flow Batteries: Status and Challenges. *ACS Energy Letters* 2, 9, 2187-2204.

47. Zhong, F.; Yang, M.; Ding, M.; Jia, C., (2020). Organic Electroactive Molecule-Based Electrolytes for Redox Flow Batteries: Status and Challenges of Molecular Design. *Frontiers in Chemistry* 8, 451.

48. Figgener, J.; Stenzel, P.; Kairies, K.-P.; Linßen, J.; Haberschusz, D.; Wessels, O.; Angenendt, G.; Robinius, M.; Stolten, D.; Sauer, D. U., (2020). The development of stationary battery storage systems in Germany – A market review. *Journal of Energy Storage* 29, 101153.

49. Wedege, K.; Drazevic, E.; Konya, D.; Bentien, A., (2016). Organic Redox Species in Aqueous Flow Batteries: Redox Potentials, Chemical Stability and Solubility. *Sci Rep* 6, 39101.

50. Er, S.; Suh, C.; Marshak, M. P.; Aspuru-Guzik, A., (2015). Computational design of molecules for an all-quinone redox flow battery. *Chem Sci* 6, 2, 885-893.

51. Dieterich, V.; Milshtein, J. D.; Barton, J. L.; Carney, T. J.; Darling, R. M.; Brushett, F. R., (2018). Estimating the cost of organic battery active materials: a case study on anthraquinone disulfonic acid. *Translational Materials Research* 5, 3, 034001-034018.

52. Wiberg, C.; Carney, T. J.; Brushett, F.; Ahlberg, E.; Wang, E., (2019). Dimerization of 9,10-anthraquinone-2,7-Disulfonic acid (AQDS). *Electrochim. Acta* 317, 478-485.

53. Carney, T. J.; Collins, S. J.; Moore, J. S.; Brushett, F. R., (2017). Concentration-Dependent Dimerization of Anthraquinone Disulfonic Acid and Its Impact on Charge Storage. *Chem. Mater.* 29, 11, 4801-4810.

54. Gerhardt, M. R.; Tong, L.; Gómez-Bombarelli, R.; Chen, Q.; Marshak, M. P.; Galvin, C. J.; Aspuru-Guzik, A.; Gordon, R. G.; Aziz, M. J., (2017). Anthraquinone Derivatives in Aqueous Flow Batteries. *Advanced Energy Materials* 7, 8, 1601488.

55. Pineda Flores, S. D.; Martin-Noble, G. C.; Phillips, R. L.; Schrier, J., (2015). Bio-Inspired Electroactive Organic Molecules for Aqueous Redox Flow Batteries. 1. Thiophenoquinones. *The Journal of Physical Chemistry C* 119, 38, 21800-21809.

56. Kwabi, D. G.; Lin, K.; Ji, Y.; Kerr, E. F.; Goulet, M.-A.; De Porcellinis, D.; Tabor, D. P.; Pollack, D. A.; Aspuru-Guzik, A.; Gordon, R. G.; Aziz, M. J., (2018). Alkaline Quinone Flow Battery with Long Lifetime at pH 12. *Joule* 2, 9, 1894-1906.

57. Gentil, S.; Reynard, D.; Girault, H. H., (2020). Aqueous organic and redox-mediated redox flow batteries: a review. *Current Opinion in Electrochemistry* 21, 7-13.

58. Chen, R., (2020). Redox flow batteries for energy storage: Recent advances in using organic active materials. *Current Opinion in Electrochemistry* 21, 40-45.

59. Kwabi, D. G.; Ji, Y.; Aziz, M. J., (2020). Electrolyte Lifetime in Aqueous Organic Redox Flow Batteries: A Critical Review. *Chem. Rev.* 120, 14, 6467-6489.

60. Bhosale, S. V.; Jani, C. H.; Langford, S. J., (2008). Chemistry of naphthalene diimides. *Chem. Soc. Rev.* 37, 2, 331-342.

61. Shukla, J.; Mukhopadhyay, P., (2019). Synthesis of Functionalized Naphthalene Diimides and their Redox Properties. *Eur. J. Org. Chem.* 2019, 48, 7770-7786.

62. Zong, L.; Xie, Y.; Wang, C.; Li, J.-R.; Li, Q.; Li, Z., (2016). From ACQ to AIE: the suppression of the strong π - π interaction of naphthalene diimide derivatives through the adjustment of their flexible chains. *Chem. Commun.* 52, 77, 11496-11499.

63. Medabalmi, V.; Sundararajan, M.; Singh, V.; Baik, M.-H.; Byon, H. R., (2020). Naphthalene diimide as a two-electron anolyte for aqueous and neutral pH redox flow batteries. *Journal of Materials Chemistry A* 8, 22, 11218-11223.

64. Wiberg, C.; Owusu, F.; Wang, E.; Ahlberg, E., (2019). Electrochemical Evaluation of a Napthalene Diimide Derivative for Potential Application in Aqueous Organic Redox Flow Batteries. *Energy Technology* 7, 11.

65. Kowalski, J. A.; Su, L.; Milshtein, J. D.; Brushett, F. R., (2016). Recent advances in molecular engineering of redox active organic molecules for nonaqueous flow batteries. *Current Opinion in Chemical Engineering* 13, 45-52.

66. Milshtein, J. D.; Kaur, A. P.; Casselman, M. D.; Kowalski, J. A.; Modekrutti, S.; Zhang, P. L.; Harsha Attanayake, N.; Elliott, C. F.; Parkin, S. R.; Risko, C.; Brushett, F. R.; Odom, S. A., (2016). High current density, long duration cycling of soluble organic active species for non-aqueous redox flow batteries. *Energy & Environmental Science* 9, 11, 3531-3543.

67. Wang, Q.; Mao, B.; Stoliarov, S. I.; Sun, J., (2019). A review of lithium ion battery failure mechanisms and fire prevention strategies. *Prog. Energy Combust. Sci.* 73, 95-131.

68. Huisman, J.; Ciuta, T.; Mathieux, F.; Bobba, S.; Georgitzikis, K.; Pennington, D. *RMIS – Raw materials in the battery value chain*; 2020.

69. Helbig, C.; Bradshaw, A. M.; Wietschel, L.; Thorenz, A.; Tuma, A., (2018). Supply risks associated with lithium-ion battery materials. *Journal of Cleaner Production* 172, 274-286.

70. Watari, T.; McLellan, B. C.; Giurco, D.; Dominish, E.; Yamasue, E.; Nansai, K., (2019). Total material requirement for the global energy transition to 2050: A focus on transport and electricity. *Resources, Conservation and Recycling* 148, 91-103.

71. Al Barazi, S. *Rohstoffrisikobewertung – Kobalt. – DERA Rohstoffinformationen 36: 120 S.*; Deutsche Rohstoffagentur: Berlin, 2018.

72. Otamonga, J.-P.; Poté, J. W., (2020). Abandoned mines and artisanal and small-scale mining in Democratic Republic of the Congo (DRC): Survey and agenda for future research. *Journal of Geochemical Exploration* 208, 106394.

73. Price, J., (2019). Opportunities in global mineral resources. *BOLETÍN GEOLÓGICO Y MINERO* 130, 47-56.

74. Minke, C.; Dorantes Ledesma, M. A., (2019). Impact of cell design and maintenance strategy on life cycle costs of vanadium redox flow batteries. *Journal of Energy Storage* 21, 571-580.

75. Hammond, A. D., (2016). Vanadium trends in exploration; markets and future demands. *Mining Engineering* 68, 8, 27-30.

76. Yaroshevsky, A. A., (2006). Abundances of chemical elements in the Earth's crust. *Geochemistry International* 44, 1, 48-55.

77. Elgrishi, N.; Rountree, K. J.; McCarthy, B. D.; Rountree, E. S.; Eisenhart, T. T.; Dempsey, J. L., (2017). A Practical Beginner's Guide to Cyclic Voltammetry. *J. Chem. Educ.* 95, 2, 197-206.

78. Goldsmith, J. I.; Takada, K.; Abruna, H. D., (2002). Probing diffusional transport in redox-active dendrimers. *J. Phys. Chem. B* 106, 34, 8504-8513.

79. Tourwé, E.; Breugelmans, T.; Pintelon, R.; Hubin, A., (2007). Extraction of a quantitative reaction mechanism from linear sweep voltammograms obtained on a rotating disk electrode. Part II: Application to the redoxcouple. *J. Electroanal. Chem.* 609, 1, 1-7.

80. Scholz, F.; Bond, A. M., *Electroanalytical methods : guide to experiments and applications*. 2nd, rev. and extended ed.; Springer: Heidelberg ; New York, 2010; p xxvii, 359 p.

81. Bard, A. J.; Faulkner, L. R., *Electrochemical methods : fundamentals and applications*. 2nd ed.; Wiley: New York, 2001; p xxi, 833 p.

82. Zanello, P.; Royal Society of Chemistry (Great Britain), *Inorganic electrochemistry : theory, practice and applications*. Royal Society of Chemistry: Cambridge, 2003; p xiv, 615 p.

83. Compton, R. G.; Banks, C. E., *Understanding voltammetry*. Third edition. ed.; World Scientific: New Jersey, 2018; p xvi, 439 pages.

84. Gandomi, Y. A.; Aaron, D. S.; Houser, J. R.; Daugherty, M. C.; Clement, J. T.; Pezeshki, A. M.; Ertugrul, T. Y.; Moseley, D. P.; Mench, M. M., (2018). Critical Review—Experimental Diagnostics and Material Characterization Techniques Used on Redox Flow Batteries. *J. Electrochem. Soc.* 165, 5, A970-A1010.

85. Lasia, A., *A. Lasia, Electrochemical Impedance Spectroscopy and its Applications, book, Springer, 2014*. 2014.

86. Le Chatelier, H., (1891). Sur les transformations moléculaires des métaux et leurs conductibilités électriques. *J. Phys. Theor. Appl.* 10, 1, 369-374.

87. Batchelor-McAuley, C.; Li, Q.; Dapin, S. M.; Compton, R. G., (2010). Voltammetric characterization of DNA intercalators across the full pH range: anthraquinone-2,6-disulfonate and anthraquinone-2-sulfonate. *J. Phys. Chem. B* 114, 11, 4094-100.

88. Rosso, K. M.; Smith, D. M. A.; Wang, Z. M.; Ainsworth, C. C.; Fredrickson, J. K., (2004). Self-exchange electron transfer kinetics and reduction potentials for anthraquinone disulfonate. *J. Phys. Chem. A* 108, 16, 3292-3303.

89. Seralathan, M.; Rangarajan, S. K., (1985). Scheme of squares: Part I. Systems formalism for potentiostatic studies. *Journal of Electroanalytical Chemistry and Interfacial Electrochemistry* 191, 2, 209-228.

90. Quan, M.; Sanchez, D.; Wasylkiw, M. F.; Smith, D. K., (2007). Voltammetry of Quinones in Unbuffered Aqueous Solution: Reassessing the Roles of Proton Transfer and Hydrogen Bonding in the Aqueous Electrochemistry of Quinones. *J. Am. Chem. Soc.* 129, 42, 12847-12856.

91. Price, W. S., (1997). Pulsed-field gradient nuclear magnetic resonance as a tool for studying translational diffusion: Part 1. Basic theory. *Concepts in Magnetic Resonance* 9, 5, 299-336.

92. Frueh, D. P., (2014). Practical aspects of NMR signal assignment in larger and challenging proteins. *Prog. Nucl. Magn. Reson. Spectrosc.* 78, 47-75.

93. Cubberley, M. S.; Iverson, B. L., (2001). 1H NMR Investigation of Solvent Effects in Aromatic Stacking Interactions. *J. Am. Chem. Soc.* 123, 31, 7560-7563.

94. Bain, A. D., Chemical Exchange Effects in NMR. In *Encyclopedia of Spectroscopy and Spectrometry*, Lindon, J. C., Ed. Elsevier: Oxford, 1999; pp 198-207.

95. Chen, J. S.; Shirts, R. B., (1985). Iterative determination of the NMR monomer shift and dimerization constant in a self-associating system. *The Journal of Physical Chemistry* 89, 9, 1643-1646.

96. Einstein, A., (1905). Über einen die Erzeugung und Verwandlung des Lichtes betreffenden heuristischen Gesichtspunkt. *Annalen der Physik* 322, 6, 132-148.

97. Arons, A. B.; Peppard, M. B., (1965). Einstein's Proposal of the Photon Concept—a Translation of the Annalen der Physik Paper of 1905. *American Journal of Physics* 33, 5, 367-374.

98. Schrödinger, E., (1926). An Undulatory Theory of the Mechanics of Atoms and Molecules. *Physical Review* 28, 6, 1049-1070.

99. Schrödinger, E., (1926). Quantisierung als Eigenwertproblem. *Annalen der Physik* 384, 4, 361-376.

100. Hartree, D. R., (1928). The Wave Mechanics of an Atom with a Non-Coulomb Central Field. Part II. Some Results and Discussion. *Mathematical Proceedings of the Cambridge Philosophical Society* 24, 1, 111-132.

101. Slater, J. C., (1928). The Self Consistent Field and the Structure of Atoms. *Physical Review* 32, 3, 339-348.

102. Fock, V., (1930). Näherungsmethode zur Lösung des quantenmechanischen Mehrkörperproblems. *Zeitschrift für Physik* 61, 1, 126-148.

103. Kohn, W.; Sham, L. J., (1965). Self-Consistent Equations Including Exchange and Correlation Effects. *Physical Review* 140, 4A, A1133-A1138.

104. Kim, M. B.; Dixon, D. W., (2008). Hydrolysis of aliphatic naphthalene diimides: effect of charge placement in the side chains. *J. Phys. Org. Chem.* 21, 9, 731-737.

105. Wei, L.; Zhao, T. S.; Xu, Q.; Zhou, X. L.; Zhang, Z. H., (2017). In-situ investigation of hydrogen evolution behavior in vanadium redox flow batteries. *Applied Energy* 190, 1112-1118.

106. Oregioni, A.; Stieglitz, B.; Kelly, G.; Rittinger, K.; Frenkiel, T., (2017). Determination of the pKa of the N-terminal amino group of ubiquitin by NMR. *Sci Rep* 7, 43748.

107. Tong, L.; Chen, Q.; Wong, A. A.; Gomez-Bombarelli, R.; Aspuru-Guzik, A.; Gordon, R. G.; Aziz, M. J., (2017). UV-Vis spectrophotometry of quinone flow battery electrolyte for in situ monitoring and improved electrochemical modeling of potential and quinhydrone formation. *Phys. Chem. Chem. Phys.* 19, 47, 31684-31691.

108. Nibel, O.; Taylor, S. M.; Pătru, A.; Fabbri, E.; Gubler, L.; Schmidt, T. J., (2017). Performance of Different Carbon Electrode Materials: Insights into Stability and Degradation under Real Vanadium Redox Flow Battery Operating Conditions. *J. Electrochem. Soc.* 164, 7, A1608-A1615.